COVERAGE OPTIMIZATION FOR 6G USING RECONFIGURABLE INTELLIGENT SURFACES

by

Samed Keşir

B.S., Electrical Electronics Engineering, Boğaziçi University, 2020

Submitted to the Institute for Graduate Studies in
Science and Engineering in partial fulfillment of
the requirements for the degree of
Master of Science

Graduate Program in Electrical Electronics Engineering
Boğaziçi University

2023

ACKNOWLEDGEMENTS

First and foremost, I would like to express my sincere gratitude to my advisor, Prof. Ali Emre Pusane, for his guidance, support, and encouragement throughout my research. His expertise and insights were invaluable in shaping my ideas and refining my work. I am genuinely grateful for his patience and generosity and the opportunity to learn from him.

I would like to thank my beloved wife, Fatma Nur, for her unwavering love, understanding, and encouragement during this journey. Her patience, support, and motivation helped me overcome problems and remain focused on my goals. I could not have done this without her.

I would like to extend my gratitude to my parents for their constant love, support, and encouragement throughout my life. Their endless belief in me has been a source of strength and inspiration, and I am forever grateful for their sacrifices and guidance.

Finally, I want to acknowledge my colleagues and friends at TÜBİTAK Bilgem Hisar Lab. who have provided me with guidance, advice, and support throughout my research. Their feedback, encouragement, and company made this journey more meaningful and enjoyable. I am fortunate to have had the opportunity to work with such talented and dedicated individuals, and I look forward to continuing our collaboration in the future.

ABSTRACT

COVERAGE OPTIMIZATION FOR 6G USING RECONFIGURABLE INTELLIGENT SURFACES

Recent research has shown that a reconfigurable intelligent surface (RIS), which is an attractive technology due to its low complexity and power requirements, can considerably improve the performance of wireless communication systems. RIS composed of small, reconfigurable, passive elements can be programmed to reflect the signal in a particular direction, amplify or attenuate it, or even introduce additional signal components to improve the overall communication performance. RIS can be utilized for different purposes including enhancements to the coverage, positioning, capacity, security, and sustainability. In this thesis, coverage enhancement and the physical layer security (PLS) use cases of RIS are investigated. For the coverage enhancement, single-user and two-user scenarios are discussed. In the single-user scenario, a RIS optimization method using Convolutional Neural Networks (CNN) is proposed to reduce the number of iterations required for optimization. The results show that the proposed CNN model significantly decreases the number of steps required for the configuration by causing a slight degradation in the performance. In the two-user scenario, both coverage enhancement and security use cases are investigated. For coverage enhancement, it is shown that the RIS gain distribution between the users can be managed with respect to the needs by configuring the RIS accordingly. For the security use case, measurement-based characterization of RIS for providing physical layer security, where the transmitter (Alice), the intended user (Bob), and the eavesdropper (Eve) are deployed in an indoor environment is presented. Also, the measurement results are verified with the simulation results. Finally, a thresholding method is proposed to prevent Eve's dominance in PLS and provide more RIS gain to Bob in return for a slight reduction in secrecy capacity.

ÖZET

YENİDEN YAPILANDIRILABİLİR AKILLI YÜZEYLER KULLANARAK 6G İÇİN KAPSAM OPTİMİZASYONU

Yeniden yapılandırılabilir akıllı yüzeyin (RIS) düşük karmaşıklık ve güç gereksinimleri nedeniyle kablosuz iletişim sistemlerinin performansını önemli ölçüde artırabileceği görülmektedir. Küçük, yapılandırılabilir, pasif öğelerden oluşan RIS'ler, sinyali belirli bir yönde yansıtmak, yükseltmek, zayıflatmak ve genel iletişim performansını iyileştirmek için ek sinyal bileşenleri eklemek üzere programlanabilir. RIS'ler, kapasite, kapsam, konumlandırma, güvenlik ve sürdürülebilirlik iyileştirmeleri dahil olmak üzere farklı amaçlar için kullanılabilir. Bu tez çalışmasında, RIS'in kapsam geliştirme ve fiziksel katman güvenliği (PLS) kullanım durumları incelenmiştir. Kapsam geliştirme için tek kullanıcılı ve iki kullanıcılı senaryolar ele alınmıştır. Tek kullanıcı senaryosunda, optimizasyon için gerekli yineleme sayısını azaltmak için Konvolüsyonel Sinir Ağları (CNN) kullanan bir RIS optimizasyon yöntemi önerilmiştir. Sonuçlar, önerilen CNN modelinin performansta hafif bir düşüş karşılığında yapılandırma için gerekli adım sayısını önemli ölçüde azalttığını göstermektedir. İki kullanıcılı senaryoda, hem kapsam geliştirme hem de güvenlik kullanım durumları incelenmiştir. Kapsam iyileştirme için, RIS buna göre yapılandırılarak kullanıcılar arasındaki RIS kazanç dağılımının ihtiyaca göre yönetilebileceği gösterilmiştir. Güvenlik kullanım durumu için, vericinin (Alice), kullanıcının (Bob) ve dinleyicinin (Eve) bir iç mekan ortamındayken PLS sağlamaya yönelik RIS'in ölçüme dayalı karakterizasyonu sunulmuştur. Ayrıca, ölçüm sonuçları simülasyon sonuçları ile doğrulanmıştır. Son olarak, Eve'in PLS'deki hakimiyetini önlemek ve gizlilik kapasitesinde hafif bir azalma karşılığında Bob'a daha fazla RIS kazancı sağlamak için bir eşikleme yöntemi önerilmiştir.

TABLE OF CONTENTS

ACKNOWLEDGEMENTS iii
ABSTRACT iv
ÖZET v
LIST OF FIGURES viii
LIST OF TABLES xii
LIST OF SYMBOLS xiii
LIST OF ACRONYMS/ABBREVIATIONS xiv
1. INTRODUCTION 1
1.1. Related Work 7
1.2. Thesis Contribution 12
1.3. Thesis Organization 12
2. SYSTEM MODEL 14
2.1. Single-User Communication Scenario 14
2.2. Two-User Communication Scenario 17
3. CNN-BASED OPTIMIZATION APPROACH 21
3.1. Iterative Phase 21
3.2. CNN Model 25
3.3. Results of the CNN-Based Optimization Approach 27
4. COVERAGE OPTIMIZATION IN THE PRESENCE OF ANOTHER USER 32
4.1. Simultaneous Coverage Enhancement of Both Users 32
4.1.1. Fair Coverage Enhancement of Both Users 32
4.1.2. Prioritized Coverage Enhancement of Both Users 34
4.1.3. Results of Simultaneous Coverage Enhancement of Both Users . 34
4.1.3.1. Results of Fair Power Distribution 38
4.1.3.2. Results of Prioritized Power Distribution 39
4.2. Coverage Enhancement of One User by Mitigating The Interference for Other 41
4.2.1. Optimal Secrecy Capacity Maximization 41

4.2.2. Sub-optimal Secrecy Capacity Maximization 43
4.2.3. Results of Coverage Optimization and Interference Minimization Simultaneously 45
4.2.3.1. Results for Optimal Secrecy Capacity Maximization . 45
4.2.3.2. Results for Sub-optimal Secrecy Capacity Maximization 53
5. CONCLUSION 55
5.1. Future Work 56
REFERENCES 58

LIST OF FIGURES

Figure 1.1. Coverage enhancement of a modem via RIS in an office environment. 6

Figure 2.1. An RIS-assisted wireless communication system for a single-user communication scenario. 15

Figure 2.2. An RIS-assisted wireless communication system for a two-user communication scenario. 18

Figure 3.1. The classical iterative algorithm for the RIS optimization. 22

Figure 3.2. The modified iterative algorithm for configuring RIS elements horizontally and vertically for dataset generation. 23

Figure 3.3. Configuration found by searching the optimum configuration for (a) $\varphi = 0^\circ$ beam planes, (b) $\varphi = 90^\circ$ beam planes, and (c) all beam space. (d), (e), and (f) give the radiation patterns of the corresponding configuration. 24

Figure 3.4. The CNN architecture illustration. 26

Figure 3.5. (a) Estimated configuration of the proposed CNN model and (b) the radiation pattern of this configuration. 28

Figure 3.6. The distribution of the power differences between the iterative method and the proposed method over the angular position of the receiver. 28

Figure 3.7. The illustration of the real configurations ((a), (c)) and their estimated configurations ((b), (d)) for $\vartheta = 0°, \varphi = 0°$ and $\vartheta = 60°, \varphi = 300°$, respectively. 29

Figure 3.8. The distribution of the power differences between the iterative method and the horizontal and vertical stripe grouping method over the angular position of the receiver. 30

Figure 3.9. (a) The configuration found according to the algorithm given in [29] and (b) the radiation pattern of this configuration. 31

Figure 4.1. The modified iterative algorithm for coverage optimization for two-user through RIS. 33

Figure 4.2. Scattered radiation pattern of the RIS before any phase optimization (a) in terms of azimuth and elevation angles and (b) in terms of cartesian coordinates. 35

Figure 4.3. When the coverage optimization is applied by considering only the first receiver, (a) resulting configuration of the RIS (b) the received power levels with respect to iterations. 36

Figure 4.4. Scattered radiation pattern of the RIS when the coverage optimization is applied by considering only the first receiver (a) in terms of azimuth and elevation angles and (b) in terms of cartesian coordinates. 37

Figure 4.5. When the coverage optimization is applied by considering the receivers in a fair way, (a) resulting configuration of the RIS (b) the received power levels with respect to iterations. 38

Figure 4.6. Scattered radiation pattern of the RIS after the fair coverage optimization for two receivers (a) in terms of azimuth and elevation angles and (b) in terms of cartesian coordinates. 39

Figure 4.7. When the coverage optimization is applied by considering the receivers by prioritizing Rx_2, (a) resulting configuration of the RIS (b) the received power levels with respect to iterations. 40

Figure 4.8. Scattered radiation pattern of the RIS after the prioritized coverage optimization for two receivers (a) in terms of azimuth and elevation angles and (b) in terms of cartesian coordinates. 40

Figure 4.9. The modified iterative algorithm for secrecy capacity maximization. 43

Figure 4.10. The modified iterative algorithm for secrecy capacity maximization with thresholding method. 44

Figure 4.11. Scattered radiation pattern of the RIS after the coverage optimization with interference minimization (a) in terms of azimuth and elevation angles and (b) in terms of cartesian coordinates. 46

Figure 4.12. When the coverage optimization is applied by considering maximization of the secrecy capacity, (a) resulting configuration of the RIS (b) the received power levels with respect to iterations. 47

Figure 4.13. Simulation results of the received powers when the objective is to maximize the secrecy capacity. 47

Figure 4.14. Simulation results of received power of (a) Bob when the objective is to maximize the received power, (b) Eve when the objective is to minimize the received power. 48

Figure 4.15. The measurement setup of the RIS-assisted wireless communication system. 49

Figure 4.16. Measurement results of the received powers when the objective is to maximize the secrecy capacity. 51

Figure 4.17. Measurement results of received power of (a) Bob when the objective is to maximize the received power, (b) Eve when the objective is to minimize the received power. 52

Figure 4.18. Scattered radiation pattern of the RIS after the coverage optimization with interference minimization under the threshold constraint (a) in terms of azimuth and elevation angles and (b) in terms of cartesian coordinates. 53

Figure 4.19. When the coverage optimization is applied by considering maximization of the secrecy capacity with the constraint of a threshold to the unintended receiver, (a) resulting configuration of the RIS (b) the received power levels with respect to iterations. 54

LIST OF TABLES

Table 3.1. The proposed CNN model architecture. 25

Table 4.1. The locations of Alice, Bob, and Eve in meters. 50

LIST OF SYMBOLS

A_{mn}	Illuminating amplitude of the signal coming to the element
d_x	Distance between adjacent element in x direction
d_y	Distance between adjacent element in y direction
f	The radiation pattern of the microstrip patch antenna
$\mathbf{g}$	Channel from receiver to the RIS in vector form
g_{mn}	Channel from $(m,n)^{th}$ element of the RIS to the receiver
$\mathbf{h}$	Channel from transmitter to the RIS in vector form
h_{mn}	Channel from transmitter to $(m,n)^{th}$ element of the RIS
n	Noise component
N	Noise power
P_{rx}	Received power
P_{tx}	Transmitted power
pl_{mn}	Path loss function
R_{mn}^{tx}	Distance from transmitter to the $(m,n)^{th}$ element of the RIS
R_{mn}^{rx}	Distance from receiver to the $(m,n)^{th}$ element of the RIS
x	Transmitted complex baseband signal
y_{rx}	Received signal at the receiver side
α_{mn}	Illuminating phase of the signal coming to the element
Γ_{mn}	Reflection amplitude of the $(m,n)^{th}$ element of the RIS
λ	Wavelength of the input signal
ϕ_{mn}	Reflection phase of the $(m,n)^{th}$ element of the RIS
$\mathbf{\Theta}$	Reflection phases of the the RIS in matrix form
φ	Variable azimuth
φ_{mn}	Azimuth angle of the transmitter to the element
ϑ	Variable elevation
ϑ_{mn}	Elevation angle of the transmitter to the element

LIST OF ACRONYMS/ABBREVIATIONS

2D	Two Dimensional
3D	Three Dimensional
5G	Fifth-Generation
6G	Sixth-Generation
AP	Access Point
CNN	convolutional Neural Network
CSI	channel State Information
DRL	Deep Reinforcement Learning
EE	Energy Efficiency
EM	Electromagnetic
IRS	Intelligent Reflecting Surface
KPI	Key Performance Index
LOS	Line-of-Sight
MIMO	Multiple Input Multiple Output
mmWave	Millimeter Wave
NLOS	Non-Line-of-Sight
NOMA	Non Orthogonal Multiple Access
OFDM	Orthogonal Frequency Division Multiplexing
PLS	Physical Layer Security
QoS	Quality of Service
RIS	Reconfigurable Intelligent Surface
RSSI	Received Signal Strength Indicator
SE	Spectral Efficiency
SINR	signal-to-Interference plus Noise Ratio
SNR	Signal-to-Noise Ratio
SRE	Smart Radio Environment
VNA	Vector Network Analyzer

1. INTRODUCTION

Beyond 5G communications, which aims to meet more demanding requirements than 5G, such as ultra-high data rates, energy efficiency (EE), global coverage and connectivity, spectral efficiency (SE), as well as high reliability and low air latency, is generating excitement in both academia and industry. Providing advanced multimedia services to a large number of users will require improved overall network performance, including targeting higher coverage and spectral efficiency. It is therefore essential to develop new and innovative technologies sustainably to enable future wireless network capacity increases with moderate budgets, complexity, and energy consumption, and can be managed along with the widespread adoption of user devices. On the other hand, the time-varying radio channel due to user mobility poses a major challenge in building reliable wireless communications. Either employing various modulation, coding, and diversity plans to account for channel fading, or adapting to it by using adjusted power, rate control, and beamforming techniques, are the traditional solutions to this issue [1].

As overall improvement is still limited and the current modern physical layer solutions are inadequate, novel and innovative physical layer solutions are required. To fulfill the goal of the quality of service (QoS) and the simplicity of the transceiver components, innovative communication patterns that utilize randomness of the propagation environment are gaining interest. Academic scholars have recently integrated reconfigurable intelligent surface (RIS) into wireless communications [2]. The RIS makes the wireless environment flexible and adjustable, which is a key step in realizing the notion of smart radio environments (SREs).

A reconfigurable intelligent surface, sometimes referred to as an intelligent reflecting surface (IRS), an affordable surface that may be a lightweight composite structural layer, is a configurable surface that can be utilized to alter the radiation of electromagnetic (EM) waves by modifying the surface's magnetic and electric properties. Low

implementation costs and energy consumption are achieved by using mostly passive components instead of expensive active components like power amplifiers. Hence, RIS deployment is simple and adaptable, with the ability for RIS to take any shape and be integrated into objects. Since RIS are designed to operate as practically passive devices, they are not likely to cause a rise in EM field vulnerability and may even be used to lessen it in legacy deployments. These corresponding traits imply that RIS might be taken into account as a green, environmentally friendly technology option. Depending on elements like price, form factor, design, and integration, RIS structures can change.

Implementing RIS can be done through the use of metamaterials and meta-surfaces. Metamaterials are synthetic materials with engineered properties. Usually, they are created through the synthesis of several components made of composite materials like metals and plastics. It is possible to achieve the desired transformation of transmitted, reflected, or received EM waves by using a thin metamaterial layer, also known as a meta-surface. Unit cells are typically arranged in a meta-surface at regular intervals. Using different components integrated into the surface, such as varactor diodes, PIN diodes, and liquid crystals, the EM properties of a meta-surface may be electronically tuned. Besides, elementary antennas are used as reflecting elements in reflectarrays. A load connected to an antenna element, for example, can be changed to alter the reflection specifications, such as the phase delays, of the elements. By choosing the appropriate phase responses of the adjacent array elements, a phase gradient can be created on the array to control the reflection of the impinging electromagnetic wave. As a result, RIS units can be implemented using reflectarrays. Reflectarrays frequently behave as meta-surfaces when the element spacing is decreased and antenna elements are changed.

There are various RIS circuit designs available. RIS can be viewed as a general-purpose piece of hardware, encompassing everything from meta-surfaces that can control wave propagation in extremely dense scattering environments to those that can achieve desired anomalous reflection outside the realm of the well-known Snell's law [3].

RIS can be made to function in a variety of modes while exhibiting energy efficiency that is on par with that of their reflective counterparts. Operating modes can be grouped under 3 categories: Active RIS, Passive RIS, and Hybrid RIS. When RF circuitry and subsequent signal processing units are integrated into RIS, the term "active RIS" is used. Furthermore, by cramming an increasing number of software-controlled antenna elements onto a two-dimensional surface of finite size, active RIS systems represent a logical evolution of conventional massive MIMO systems. When compared to passive RIS, the active RIS structure is capable of carrying out more tasks because it can be used to transmit and receive signals across the entire surface or use only a few elements. It's common to refer to a RIS structure as semi-active if only some of its components can transmit and/or receive data [4]. Active RIS is also used in practice with the discrete photonic antenna array. To transmit, receive, and convert optical or RF signals, it integrates active optical-electrical detectors, converters, and modulators.

Similar to a passive metal mirror or wave collector, passive RIS can be programmed to alter an impinging electromagnetic field in a variety of ways. In contrast to its active counterpart, a passive RIS is typically made up of inexpensive, practically passive components that do not need special power sources [5]. Energy harvesting modules can be used to power their circuitry and embedded sensors, which has the potential to make them truly energy neutral. The ability of passive RIS technology to shape radio waves impinging on it, forwarding the incoming signal without using any power amplifier or RF chain, and even without applying sophisticated signal processing, is what makes it appealing from an energy consumption standpoint. A hybrid RIS has the ability to both sense and partially reflect the impinging signal. Hybrid RIS has the potential to significantly improve coherent communications without significantly reducing the benefits of passive RIS's energy efficiency and coverage expansion [6]. A surface loaded by a varactor, whose capacitance can be altered by an external DC signal, is one example of a Hybrid RIS implementation. The phase of the reflected wave may change due to the fluctuating capacitance. In this manner, the reflected beam can be guided in the desired directions by the phase variation along the hybrid RIS.

The idea of RIS-enabled smart wireless environments initially only took into account passive RIS unit elements with minimal power consumption. Their anticipated key role depends on the surface's ability to change the reflection properties of its constituent parts, enabling programmable manipulation of incoming electromagnetic waves in a wide range of functionalities. Accurate beamforming requires the manipulation of quasi-free space beams with fine-grained control over the reflected EM field [7]. In contrast, the wave energy is statistically evenly distributed across the wireless medium in rich scattering environments. The resulting ray chaos suggests that rays affect the RIS from all possible directions rather than just one specific one. Instead of the usual goal of producing a directive beam, the objective becomes the manipulation of as many ray paths as possible. This manipulation aims to steer the field effectively while also modifying those rays to produce constructive superposition at a target location. When in reflection mode, RIS can act as a reflector in the environment, enhancing coverage, reducing interference, and boosting capacity. In the refraction mode, incident EM waves can pass through the RIS and, by varying their phase, be refracted to various target directions. The absence of a shielding layer inside the RIS panel, which allows EM waves to pass through the panel, is the primary distinction between the refraction and reflection modes [7]. Refraction mode is frequently used in outdoor to indoor transitional situations. The RIS will be used as a controllable mirror and it will focus the incident EM waves to different target areas in order to improve coverage for specific areas inside the building. The absorption mode enables RIS to have almost no output waves, which is advantageous for the information security, privacy, and interference mitigation industries. Implementing RIS on a building facade to shield electromagnetic waves is a common use case. This would isolate the electromagnetic waves of indoor and outdoor spaces or various indoor rooms from one another. The incident wave will be absorbed by the RIS plane, preventing building walls from being penetrated.

RIS is envisioned as a new wireless technology that could enable the dynamic and goal-oriented control of radio signals between a transmitter and a receiver, effectively transforming the wireless environment into a service. This has inspired a variety of potential new use cases that aim to support new wireless technology applications and

capabilities while also enhancing several different systems' key performance indexes (KPI). As well as supporting additional sensing, wireless power transfer, and ambient back-scattering capabilities, these improvements include improvements to coverage, capacity, security, positioning, and sustainability.

The wireless signal coverage is inconsistent and the issue of weak coverage frequently occurs in the actual mobile communication system because of the influence of obstacles like buildings and trees. Although weak coverage areas might be small and inconspicuous, their negative effects might be severe. It's possible that terminals in these locations won't be able to get a guaranteed quality of service (QoS) [8]. Adding more APs to areas with poor coverage is a high-cost and ineffective solution. RIS offers an affordable and simple method. LOS propagation paths between the AP and the RIS as well as between the RIS and the terminal can be established in the weak coverage area to achieve coverage enhancement by placing the RIS in the proper location. RIS arises as a fundamental building block and a key enabler for communication in these bands. By configuring their pattern, RIS can provide a LOS-equivalent channel between the two communication terminals when it does not exist. The small element sizes motivate integrating large numbers of elements in RIS that cover smaller areas [9]. A RIS allows controlling the phase of reflected waves from each element using simple and low-cost components like PN diodes [10]. With these diodes, each element can have OFF/ON states, resulting in a reflected wave with 0/180° phase shift, respectively. More complex structures have been proposed in the literature, where elements have more states with different phase shifts [11, 12]. In Figure 1.1, one of the use cases of the RIS in an indoor office environment is illustrated, where there are two RIS modules mounted on the column in the office environment to serve the users that have poor modem coverage.

The improved coverage brought about by the increased received signal power also results in improved spectral efficiency. However, there are a number of other ways a RIS can boost spectral efficiency [13]. The channel is frequently dominated by one or two paths in a variety of circumstances, for instance at higher frequencies. The

channel's available degrees of freedom increase and the spatial multiplexing rank can be raised with the addition of a RIS. A RIS can be used to suppress interference, such as co-channel and inter-cell interference, in addition to boosting the signal power and rank of the desired terminal. A RIS may be capable of signal nulling in addition to signal boosting in a specific direction.



Figure 1.1. Coverage enhancement of a modem via RIS in an office environment.

By including sensing capabilities, RIS can be employed to perceive the environment in addition to controlling EM waves. The characteristics of the radio channels

can be partially adjusted by adding intelligent surfaces to the environment where wireless systems are functioning. The standard wireless system design paradigm, in which the radio channel is viewed as an unmanageable entity that distorts the transmitted signals, is altered by the control of radio channels. The use of intelligent surfaces can increase the energy effectiveness and stability of wireless systems. The scenarios that have been envisioned range from situations where a single RIS is mounted on a wall to guide signals arriving from a base station, for example, to a setting where nearly all surfaces (such as walls, furniture, clothes, etc.) are covered with RIS [14–16].

Aside from the fabrication, design improvements, operation modes, and use cases of the RIS, one of the trending topics in the communication society, configuration optimization, is addressed in the scope of this thesis. The detailed review is therefore provided in the following section.

1.1. Related Work

In algorithm development for RIS-aided systems, the elements within the RIS are typically modeled to function independently of each other and there is no mutual coupling between the RIS elements. This means that these theoretical results and algorithms can be applied to antenna array-based reflectors. Furthermore, reflectors are often simply modeled as linear arrays. In performance studies, the effect of array geometry on RIS reflectance behavior is negligible. However, to apply a two-dimensional array algorithm, the shape of the array is needed to be considered.

In [17], alternating optimization is used to determine the transmit covariance matrix and RIS element's phase values maximizing the channel capacity of a RIS-assisted multiple-input-multiple-output (MIMO) link. A RIS with 20 components improved the possible rate performance in a MIMO orthogonal-frequency-division-multiplexing (OFDM) link under frequency-selective channel conditions by 38.8% in the numerical examples in [17]. In [18], the authors study the application of a RIS in orthogonal and non-orthogonal multiple access (NOMA) techniques and characterize the capacity

and rate regions for both systems. The performance improvements brought about by implementing a RIS are illustrated by numerical examples. For instance, the common average rate increased by 12 dB in a two-user NOMA system. It is expected that a real-time RIS control link is necessary to attain such large advantages. Additionally, it is demonstrated that the RIS's phase control resolution for actual systems can be as low as two bits (corresponding to four phase values for the RIS elements). In [19], a combined beamforming architecture for a BS and RIS in a single-cell multi-user network employs a uniform rectangular antenna array model. The RIS in [19] has two modes that can be changed. It can be utilized for a steerable beamforming reflection or channel estimation. The results for the single-user instance demonstrated that the signal-to-noise ratio (SNR) quadratically increases with the number of RIS elements. It was shown in the multi-user instance that interference suppression using a RIS may be collaboratively constructed with the access point (AP) transmit beamforming for enhancing the performance of all system users. In addition, compared to typical systems without using the RIS, the wireless network performance can be enhanced in terms of energy consumption, coverage, and attainable rate [19].

For transmit power allocation and phase shift management in single-cell multi-user systems, in [20], the authors construct an antenna array-based RIS system, where a multi-antenna BS supports single antenna receivers. The authors propose an improved algorithm based on sequential fractional programming that approaches the optimum solution at the expense of computational complexity. Then, they compare the proposed solution with a gradient-based algorithm and relay in terms of spectral and energy efficiency. Comparing the approaches suggested in [20] to the traditional multi-antenna amplify-and-forward relaying, the energy efficiency can be improved by a factor of three. In [21], the authors assume perfect knowledge about the channel and utilize this information to solve the standard semi-definite program with existing convex optimization solvers. Infinite states are also assumed for RIS elements. While this method determines the optimum configuration for the RIS directly by a closed-form solution, it requires resource allocation for pilot signals and consumes a high computational power for channel estimation. Deep learning-based communication algorithms have

also drawn attention recently. For example, [22, 23] utilize deep reinforcement learning (DRL) for joint optimization of transmitter beamforming and RIS configuration. Besides, [24] employs federated learning to solve the multi-user case RIS optimization. Considering the difficulty of channel estimation over RIS, optimizing the RIS configuration based on the received signal strength indicator (RSSI) feedback is one of the most widely used methods in the literature. In [25], the genetic algorithm (GA) is used to optimize the RIS configuration by using the achievable sum rate feedback under a RIS-aided multi-pair communications scenario. The results show that for a small number of antenna elements in RIS, the GA is consistent with the exhaustive search.

In one practical study [26], the RIS configuration is optimized with a straightforward iterative search algorithm by measuring the transmission amplitude $|S12|$ of the vector network analyzer (VNA) for each antenna element for its all possible combinations of phase delay states and selecting the state of the element where $|S12|$ is maximized. In another practical study [27], the RIS is configured according to the feedback of the received signal power with the same algorithm at [26]. The authors in [28] use RIS in a physical layer security scenario using the same iterative search algorithm with the feedback of secrecy capacity. The RIS is utilized to increase the secrecy capacity between intended and unintended users, and simulation results were verified experimentally. Aside from these works, [27] proposes a method of grouping the elements of RIS together for decreasing the optimization time in exchange for the decline in received power gain. The optimization strategy is the same in this manner, except it is applied to each group rather than each element. In the same context, in the work of [29], RIS is configured by grouping the elements in horizontal and vertical lines in series. As a result, the total iteration number decreases significantly.

In [30], the RIS is used to improve communications from a BS with a single antenna to users with a single antenna who are close to the RIS. Allowing the RIS reflection coefficients to be dynamically modified over various time periods to produce time-varying channels for each user enables joint resource allocation to be flexible. With the use of beamforming, the RIS is utilized as a reflector in [31] to improve the

communication link. Furthermore, it utilizes spatial modulation to transmit the receiver's private information. Using the ON and OFF states, the data received by RIS is utilized to control the reflecting elements, where the reflected signal is guided by the phase changes of the components in the ON state. When an average of half of the elements are in an active state (RIS with 32×32 elements), the used beam steering increases the average SNR at the receiver by up to 9 dB. Additionally, a two-step procedure is used to get the data sent from the transmitter and RIS. The suggested methods offer a trade-off between the RIS data information rate and the attainable beamforming gain of the reflected signal. In [32], the enhancement of the signals for transmission pairs is achieved by guiding the reflected signal from an intelligent surface, while interference from other transmitters is eliminated. Along with the theoretical analysis of the potential gain of the proposed system, this paper also offers measured data. Using varactors, a 6-by-8-element array of configurable patch elements is the foundation of the intelligent surface. The interference is suppressed during the measurements using the RIS. The greatest interference suppression achievable is found to be about 30 dB, but only in a very small bandwidth. The outcomes demonstrate that interference mitigation may be accomplished using the controlled surface. The beam steering and radio resource management are based on the estimated channel state information in several of the publications looking at strategies to control the RIS [19, 20, 31].

In [33], an alternating optimization is suggested in which channel estimate is not required to manage the reflection. There, a 3200-element antenna array with a $6m^2$ array area was employed as the reflecting surface. The majority voting mechanism is used to regulate the array. The array is set up at random during the training phase such that some of the elements reflect the incident signal while others do not. The receiver updates the network with the received power at various training phases. The received power median is computed following K measurements. In particular, the element i is voted to be on if the received power is over the median more frequently while it is active than when it is off. If not, it is decided to be off. The signal processing in the transceivers is unaffected by the surface training. Additionally, the RSSI, which is typically present in virtually all wireless communication systems, reports the received

power level. The control unit of the reflecting surface receives the RSSI information. In the test situations, the transmitter's location is changed while the receiver is left in its original spot near the surface. SNR gains of these tests range from 3.8 to 20 dB, with a median of 9.5 dB.

Although the majority of RIS studies focus on theoretical aspects, measurement-based studies demonstrating the advantages of RIS-assisted wireless communication systems have been recently gaining momentum [29,34,35]. A radar cross section-based received power model for a RIS-assisted wireless communication system is presented in [34], where the proposed model is validated through the received power measurements. The path loss of a RIS-assisted communication channel is modeled in [35], where the LOS path between the transmitter and receiver is blocked. The results show that the modified models can reasonably predict the measurements. In [29], indoor and outdoor measurements are performed using a RIS prototype consisting of 1100 controllable elements, where the authors propose a RIS configuration algorithm by exploiting the geometrical array properties and the strength of the signal received at the receiver. The considered RIS provides a 26 dB power gain for indoors compared to 27 dB and 17 dB power gains over 50 m and 500 m distances for outdoors, respectively.

None of the above-mentioned measurement-based studies utilizes the RIS concept for improving physical layer security (PLS), where a theoretical framework has been presented by several papers [36–39]. For example, a RIS-assisted MIMO system is proposed for PLS assuming that the channel state information (CSI) of the legitimate user is perfectly known at the transmitter while it is not available for the eavesdropper [36]. The phase shift matrix at the RIS and the transmit covariance matrix at the transmitter are iteratively designed to minimize the transmit power so that the remaining power can be utilized to add artificial noise to suppress the eavesdroppers. The stochastic geometry theory is utilized in [37] to characterize the PLS of the downlink RIS-assisted transmission for randomly located users and a multi-antenna eavesdropper. Specifically, the authors derive an exact probability distribution of the received signal-to-interference plus noise ratio (SINR) and obtain analytical security perfor-

mance measures. The secrecy outage probability is analytically derived in [38] when the legitimate user and the eavesdropper can receive signals not only directly from the source but also from RIS. The presented analytical model successfully predicts the gain in secrecy outage probability when the number of elements in RIS increases. In [39], the secrecy rate is maximized by jointly designing active beam-forming at the base station and passive beamforming at the RIS.

1.2. Thesis Contribution

In this thesis, RIS is investigated with respect to its optimization for coverage enhancement for single-user and multi-user scenarios. The contribution of the thesis can be categorized under two main headings:

- A deep-learning supported grouping-based approach is proposed for single-user scenarios. The proposed method is applied by horizontal and vertical grouping independently to reduce the iterations number and then implementing a convolutional neural network (CNN) model to converge to the optimal solution. It is also demonstrated numerically how considerable complexity reduction may be accomplished with a minor decrement in power gain.
- A measurement-based characterization of PLS for a RIS-assisted wireless communication system is proposed for multi-user scenarios. For the measurements, a RIS prototype has been utilized in a wireless communication system in order to increase the secrecy capacity between the intended and unintended users. Besides, the measurements are verified with the simulation results. In addition, the thresholding for PLS is also proposed to prevent the decrease of unintended users' received power to become more dominant.

1.3. Thesis Organization

In Chapter 2, the system and signal model used throughout the thesis is introduced. In Chapter 3, a deep-learning supported grouping-based RIS optimization

approach is proposed and its results are analyzed by comparing with the well-known iterative algorithm. In Chapter 4, the coverage enhancement in the presence of another user is investigated from two perspectives: a) coverage enhancement for two users and b) coverage enhancement for one user by mitigating the interference for the other one. In Chapter 5, the thesis is concluded by interpreting the results and providing potential future works.

2. SYSTEM MODEL

In this chapter, the system models that this thesis is built on will be explained for single-user and two-user scenarios. The system architectures contain the transmitter, receiver(s), RIS, and blockage preventing the direct LOS channel between the transmitter and receiver(s) and requiring the utilization of the RIS to enhance the coverage for the receiver(s).

2.1. Single-User Communication Scenario

Many use cases and scenarios have been proposed in the literature to utilize RIS in next-generation communications. One of the fundamental scenarios, where RIS will have a significant role, is the case where no LOS exists between the transmitter and the receiver. This is a serious challenge at high frequencies due to poor, non-line-of-sight (NLOS) channel conditions. The RIS is intended to provide a direct reflection and beam focusing from the transmitter to the receiver to obtain high received power. The presented system model is shown in Figure 2.1, where a RIS is located on the origin of the xy-plane and faces the $+z$ direction. θ and ϕ represent the elevation and azimuth angles according to the xy-plane, respectively. The orange squares correspond to passive reflecting elements of the RIS that are controllable through the PIN diodes such that each element is responsible for adding either 0° or 180° phase delay. The PN diodes are controlled via the RIS controller by altering the amount of voltage on them. The transmitter and receiver are located in such a way that there is no direct link from the transmitter to the receiver and they only communicate through the reflected signals from the RIS.

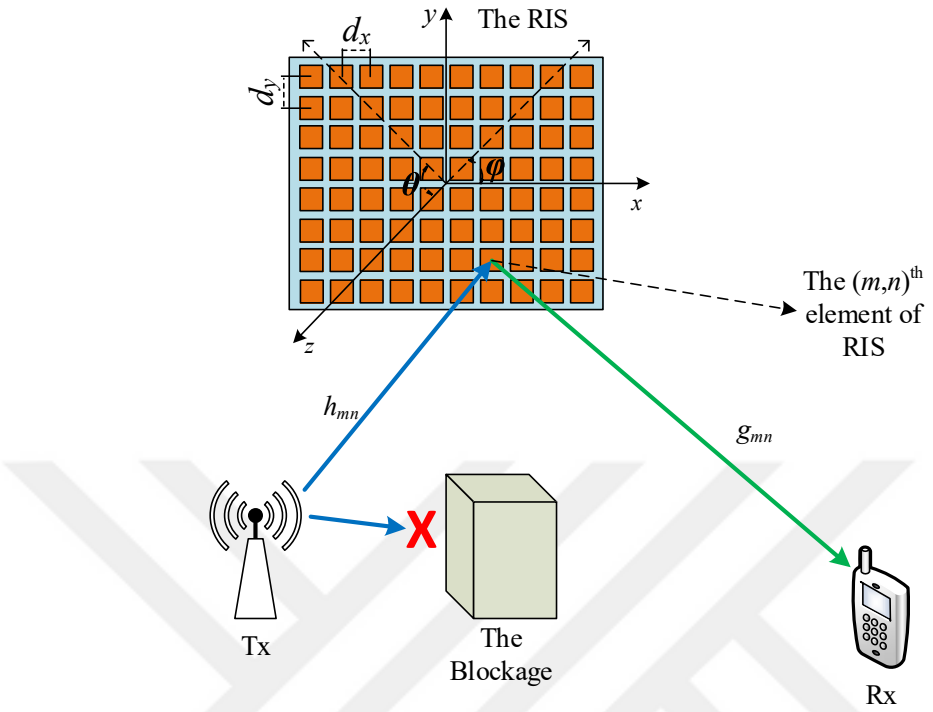

Figure 2.1. An RIS-assisted wireless communication system for a single-user communication scenario.

When the complex baseband signal $x[k]$ is transmitted, it reaches the receiver only through the RIS. The received signals at the receiver side can be expressed as

$$y_{rx}[k] = \sum_{m=0}^{M-1} \sum_{n=0}^{N-1} h_{mn} \Gamma_{mn} e^{j\phi_{mn}} g_{mn} x[k] + n[k], \tag{2.1}$$

where h_{mn} is the channel from the transmitter to the $(m,n)^{\text{th}}$ element of the RIS, while g_{mn} represents the channel from the RIS to the receiver. M and N denote the number of elements in x and y axis, respectively. Γ_{mn} and ϕ_{mn} are the reflection amplitude and phase of the $(m,n)^{\text{th}}$ element and $n[k]$ represent the noise components.

The scattering electric field of a RIS, which can be utilized to represent h_{mn} and g_{mn} using the parameters of the system model, is defined in [40] as a function of

elevation and azimuth angles (ϑ, φ) and is given as

$$E(\vartheta,\varphi) = \sum_{m=0}^{M-1}\sum_{n=0}^{N-1} A_{mn} e^{j\alpha_{mn}} f_{mn}\left(\vartheta_{mn},\varphi_{mn}\right) \Gamma_{mn} e^{j\phi_{mn}} \times f_{mn}(\vartheta,\varphi) e^{jk_0(md_x \sin\vartheta\cos\varphi + nd_y \sin\vartheta\sin\varphi)}, \tag{2.2}$$

where A_{mn} and α_{mn} are the illuminating amplitude and phase of the signal coming to the $(m,n)^{\text{th}}$ element, respectively. ϑ_{mn} and φ_{mn} denote the elevation and azimuth angles of the transmitter relative to the $(m,n)^{\text{th}}$ element, respectively. The function $f_{mn}(.)$ represents the scattering pattern of the microstrip patch antenna for the $(m,n)^{\text{th}}$ element. It is assumed that the transmitter is in the near-field of the RIS, and hence, the scattering pattern is $f_{mn}(\vartheta_{mn},\varphi_{mn}) = \cos\vartheta_{mn}$ for the incident signal, while $f_{mn}(\vartheta,\varphi) = \cos\vartheta$ for the reflected signal assuming that the receiver is in the far-field. $e^{jk_0(md_x \sin\vartheta\cos\varphi + nd_y \sin\vartheta\sin\varphi)}$ is the array steering factor of the $(m,n)^{\text{th}}$ element, where k_0 is the free-space wave-number, while d_x and d_y represent the distances between adjacent reflecting elements in x and y directions, respectively. Finally, h_{mn} and g_{mn} in (2.1) can be expressed using the components of (2.2) with the assumption of free space path loss as

$$\begin{aligned} h_{mn} =& pl_{mn}(\lambda, R_{mn}^{tx}) \cos\vartheta_{mn}, \\ g_{mn} =& pl_{mn}(\lambda, R_{mn}^{rx}) \cos\vartheta_{rx} \\ & \times e^{jk_0(md_x \sin\vartheta_{rx}\cos\varphi_{rx} + nd_y \sin\vartheta_{rx}\sin\varphi_{rx})}, \end{aligned} \tag{2.3}$$

where $pl(\lambda, R) = \frac{\lambda}{4\pi R} e^{-j2\pi R/\lambda}$ is the path loss function [1], and ϑ_{rx} and φ_{rx} are the elevation and azimuth angles of the receiver, respectively. R_{mn}^{tx} and R_{mn}^{rx} are the distances of the transmitter and the receiver to the $(m,n)^{\text{th}}$ element of RIS, respectively, and λ is the wavelength of the input signal $x[k]$.

The received signals $y_{rx}[k]$ given in (2.1) can be simply expressed using the channels in the vector forms as

$$y_{rx}[k] = \left(\mathbf{g}^H \mathbf{\Theta} \mathbf{h}\right) x[k] + n[k], \tag{2.4}$$

where

$$\begin{aligned}\mathbf{h} &= [h_{11}, h_{12}, ..., h_{mn}, ..., h_{MN}] \in \mathbb{C}^{MN\times 1},\\ \mathbf{g} &= [g_{11}, g_{12}, ..., g_{mn}, ..., g_{MN}] \in \mathbb{C}^{MN\times 1},\\ \mathbf{\Theta} &= \text{diag}\{e^{j\phi_{11}}, e^{j\phi_{12}}, ..., e^{j\phi_{mn}}, ..., e^{j\phi_{MN}}\} \in \mathbb{C}^{MN\times MN}.\end{aligned} \tag{2.5}$$

Assuming that $n[k]$ is white Gaussian noise components, the received power of the receiver (P_{rx}) can be expressed as

$$P_{rx} = \left|\mathbf{g}^H \mathbf{\Theta} \mathbf{h}\right|^2 P_{tx} + N, \tag{2.6}$$

where P_{tx} is the transmitted power from the transmitter and N is the noise power.

The received power can be increased by optimizing the phases of the RIS

$$\begin{aligned}\mathbf{\Theta}^* = \arg\max_{\phi_{mn}} &\left|\sum_{m=0}^{M-1}\sum_{n=0}^{N-1} h_{mn} e^{j\phi_{mn}} g_{mn}\right|\\ &\text{s.t. } \phi_{mn} \in \{0^\circ, 180^\circ\}, \quad \forall mn,\end{aligned} \tag{2.7}$$

where $\mathbf{\Theta}^*$ is the set of optimum phases of the RIS elements.

2.2. Two-User Communication Scenario

The system model given in Section 2.1 can be extended to multi-user models by adding other users to the system. The system model composed of two receivers is illustrated in Figure 2.2, where it is again considered that there is no line of sight between the transmitter and receivers and they only communicate via reflected signals from RIS.

When the complex baseband signal $x[k]$ is transmitted, it reaches the receiver only through the RIS. The signals received by the receivers Rx_1 and Rx_2 can be expressed as

$$\begin{aligned}y_{rx}^1[k] &= \sum_{m=0}^{M-1}\sum_{n=0}^{N-1} h_{mn}\Gamma_{mn} e^{j\phi_{mn}} g_{mn}^1 x[k] + n^1[k],\\ y_{rx}^2[k] &= \sum_{m=0}^{M-1}\sum_{n=0}^{N-1} h_{mn}\Gamma_{mn} e^{j\phi_{mn}} g_{mn}^2 x[k] + n^2[k],\end{aligned} \tag{2.8}$$

where h_{mn} represents the channel from the transmitter to the $(m,n)^{\text{th}}$ element of the RIS and it is common for both receivers. The channels from the RIS to the receivers Rx_1 and Rx_2 are represented by g^1_{mn} and g^2_{mn}, respectively. The noise components represented by $n^1[k]$ and $n^2[k]$ correspond to Rx_1 and Rx_2, respectively. The RIS parameters are assumed to be the same as those given in the system model at Section 2.1.

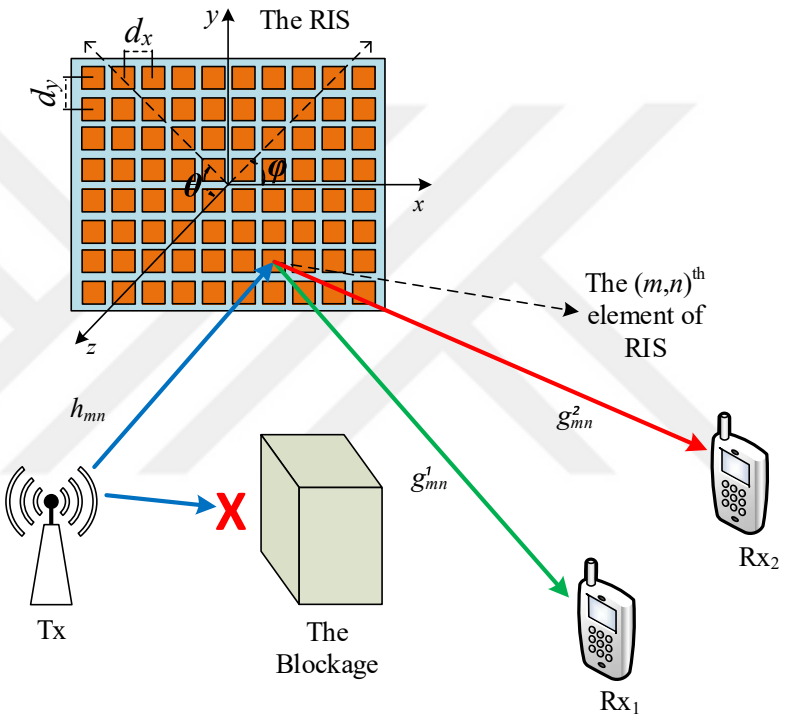

Figure 2.2. An RIS-assisted wireless communication system for a two-user communication scenario.

Using the scattering electric field given in (2.2), g^1_{mn} and g^2_{mn} in (2.8) can be openly stated using the factors of (2.2) with the same free space path loss assumption as in Section 2.1 as

$$
\begin{aligned}
g_{mn}^{1} =& pl_{mn}(\lambda, R_{mn}^{rx_1}) \cos\vartheta_{rx_1} \\
& \times e^{jk_0\left(md_x \sin\vartheta_{rx_1} \cos\varphi_{rx_1} + nd_y \sin\vartheta_{rx_1} \sin\varphi_{rx_1}\right)}, \\
g_{mn}^{2} =& pl_{mn}(\lambda, R_{mn}^{rx_2}) \cos\vartheta_{rx_2} \\
& \times e^{jk_0\left(md_x \sin\vartheta_{rx_2} \cos\varphi_{rx_2} + nd_y \sin\vartheta_{rx_2} \sin\varphi_{rx_2}\right)},
\end{aligned}
\tag{2.9}
$$

where $pl(\lambda, R) = \frac{\lambda}{4\pi R} e^{-j2\pi R/\lambda}$ is the free space path loss function [1], $(\vartheta_{rx_1},\, \varphi_{rx_1})$ and $(\vartheta_{rx_2},\, \varphi_{rx_2})$ are the elevation and azimuth angle pairs of the Rx_1 and Rx_2, respectively. R_{mn}^{tx}, $R_{mn}^{rx_1}$, and $R_{mn}^{rx_2}$ are the distances of the transmitter and the receivers to the $(\mathrm{m}, \mathrm{n})^{\mathrm{th}}$ element of RIS, respectively, and λ is the wavelength of the input signal $x[k]$.

The channel vectorization given in Section 2.1 can also be used here, hence the received signals are simply expressed as

$$
\begin{aligned}
y_{rx_1}[k] &= \left((\mathbf{g^1})^H \mathbf{\Theta h}\right) x[k] + n_1[k], \\
y_{rx_2}[k] &= \left((\mathbf{g^2})^H \mathbf{\Theta h}\right) x[k] + n_2[k],
\end{aligned}
\tag{2.10}
$$

where $\mathbf{h}$ and $\mathbf{\Theta}$ are the same as in (2.5). The terms $\mathbf{g^1}$ and $\mathbf{g^2}$ are defined as

$$
\begin{aligned}
\mathbf{g^1} &= [g_{11}^1, g_{12}^1, ..., g_{mn}^1, ..., g_{MN}^1] \in \mathbb{C}^{MN\times 1}, \\
\mathbf{g^2} &= [g_{11}^2, g_{12}^2, ..., g_{mn}^2, ..., g_{MN}^2] \in \mathbb{C}^{MN\times 1}.
\end{aligned}
\tag{2.11}
$$

With the assumption of $n^1[k]$ and $n^2[k]$ being white Gaussian noise components, the received powers of Rx_1 and Rx_2 can be written as

$$
\begin{aligned}
P_{rx_1} &= \left|(\mathbf{g^1})^H \mathbf{\Theta h}\right|^2 P_{tx} + N_1, \\
P_{rx_2} &= \left|(\mathbf{g^2})^H \mathbf{\Theta h}\right|^2 P_{tx} + N_2,
\end{aligned}
\tag{2.12}
$$

where P_{tx} represents the transmitted power from transmitter and N_1 and N_2 are the noise powers of Rx_1 and Rx_2, respectively.

Coverage optimization via RIS in the two-user communication scenario can be approached through two distinct methods. The first method entails the simultaneous enhancement of the received powers for both users. The second method involves increasing the received power of one user while mitigating potential interference by reducing the received power of the other user.

The objective of these methods can be simply expressed as

$$\begin{aligned} \mathbf{\Theta}^* = \arg\max_{\phi_{mn}} & P_{joint} \\ \text{s.t. } & \phi_{mn} \in \{0^\circ, 180^\circ\}, \quad \forall m, n, \end{aligned} \tag{2.13}$$

where P_{joint} represents the joint power of the receivers Rx_1 and Rx_2. It could be defined as $P_{joint} = P_{rx_1} + P_{rx_2}$ for a simple case.

For the first approach, it is also possible to define P_{joint} by assigning different weights to the received powers based on the level of importance given to each receiver. In the second method, P_{joint} can be defined such a way that the received power of one user is increased while the other user's received power is decreased or held around a threshold level to not lose coverage efficiency for the first user.

3. CNN-BASED OPTIMIZATION APPROACH

In this chapter, the proposed CNN-based RIS optimization approach will be investigated. The proposed method consists of two phases: a) data generation phase, and b) model design and training phase. For the first phase, the dataset comprising the RIS configurations is generated by the iterative search method [26]. The generated dataset can be divided into two: data and labels. For both data and labels, the RIS configurations are used. While for the label, the classical iterative algorithm illustrated in Figure 3.1 is employed for the configurations, the modified iterative algorithm shown in Figure 3.2 is used for the configurations used as data. Then, in the second phase, the CNN architecture is designed and the model is trained to learn the characteristics of the label configurations in terms of data configurations. Finally, the results of the proposed method will be analyzed in terms of complexity and gain performance.

3.1. Iterative Phase

A pencil-like beam pointing in a given direction $(\vartheta_{rx}, \varphi_{rx})$ can be obtained as the intersection of a vertical and a horizontal hyperplane in the beam space. By examining (2.2), it can be observed that processing the RIS elements as horizontal or vertical stripes results in a horizontal or vertical beam plane, respectively. Vertical and horizontal beam planes denote beam planes that correspond to $\varphi = 0°$ and $\varphi = 90°$, respectively. Treating the elements as stripes means configuring all the elements on the same line (with the same m or n index) with the same phase delay simultaneously. The radiation pattern has almost the same power levels along the axis parallel to the stripes and the power levels change apparently on the stripes' perpendicular axis. Additionally and with great significance, the resulting horizontal and vertical beam planes include the line pointing the user, separately. This is visually illustrated in Figure 3.3, where the configuration of the RIS in Figures 3.3 (a) and (c) are generated using the algorithm shown in Figure 3.2 while the configuration in Figures 3.3 (e) is generated by using the algorithm given in Figure 3.1. The radiation patterns in Figures 3.3 (b), (d), and (f)

result from the configurations in Figures 3.3 (a), (c), and (e) respectively. However, to obtain the beam of Figure 3.3 (f), the configuration seen in Figure 3.3 (e) can not be straightforwardly inferred from the stripe patterns.

Input: P_{rx}, M, N, and P
Output: $\mathbf{\Theta}$ (The phase shift values of the RIS elements)
initialize $\mathbf{\Theta}$ with 0° phase shift
$P_{rx}^{max} \leftarrow -\infty$
for $i \in [1, M \times N]$ **do**
  for $j \in [1, P]$ **do**
    configure ith diagonal element of $\mathbf{\Theta}$ with jth phase shift
    measure P_{rx}
    if $(P_{rx} > P_{rx}^{max})$ **then**
      update ith diagonal element of $\mathbf{\Theta}$ with jth phase shift
      $P_{rx}^{max} \leftarrow P_{rx}$
    end if
  end for
end for
return $\mathbf{\Theta}$

Figure 3.1. The classical iterative algorithm for the RIS optimization.

In this context, the first stage of the proposed algorithm aims to find the vertical and horizontal stripes iteratively depending on the feedback provided by the receiver. The ordering of this optimization (vertical/horizontal or horizontal/vertical) does not affect the results, clearly. At each iteration, a stripe of RIS elements is configured with a predefined state. The received signal power P_{rx} is then measured at the receiver, and the result is reported. According to the change in P_{rx}, the algorithm decides whether this state improves the performance of the RIS. This iteration is then repeated with a different state for the same stripe. For the RIS with $M \times N$ elements and P possible phase states for each element, this algorithm requires $(M + N) \times P$ iterations. The algorithm in Figure 3.2 gives a detailed pseudo code.

As seen in the algorithm in Figure 3.2, the output of this algorithm is two independent configurations S_h, S_v for horizontal and vertical stripes, respectively. As explained briefly in the introduction of the chapter, these two configurations form the input configurations to a CNN model that will generate a single configuration, which is expected to converge to a reference configuration generated by the algorithm in Figure 3.1, for a specific user position. In other words, the output of the CNN model is expected to generate a radiation pattern with a gain sufficiently close to that of the reference configuration in the desired $(\vartheta_{rx}, \varphi_{rx})$ direction.

Input: P_{rx}, M, N, and P
Output: S_h, S_v
initialize S_h and S_v with 0° phase shift
$P^h_{rx,max} \leftarrow -\infty$, $P^v_{rx,max} \leftarrow -\infty$
Horizontal Step List $\leftarrow$ shuffle $[1, M]$, *Vertical Step List* $\leftarrow$ shuffle $[1, N]$
for $i \in$ *Horizontal Step List* **do**
  for $j \in [1, P]$ **do**
    configure i^{th} row with j^{th} phase
    measure P_{rx}
    if $(P_{rx} > P^h_{rx,max})$ **then**
      update ith row of S_h with j^{th} phase
      $P^h_{rx,max} \leftarrow P_{rx}$
    end if
  end for
end for
for $i \in$ *Vertical Step List* **do**
  for $j \in [1, P]$ **do**
    configure i^{th} column with j^{th} phase
    measure P_{rx}
    if $(P_{rx} > P^v_{rx,max})$ **then**
      update ith column of S_v with j^{th} phase
      $P^v_{rx,max} \leftarrow P_{rx}$
    end if
  end for
end for
return S_h, S_v

Figure 3.2. The modified iterative algorithm for configuring RIS elements horizontally and vertically for dataset generation.

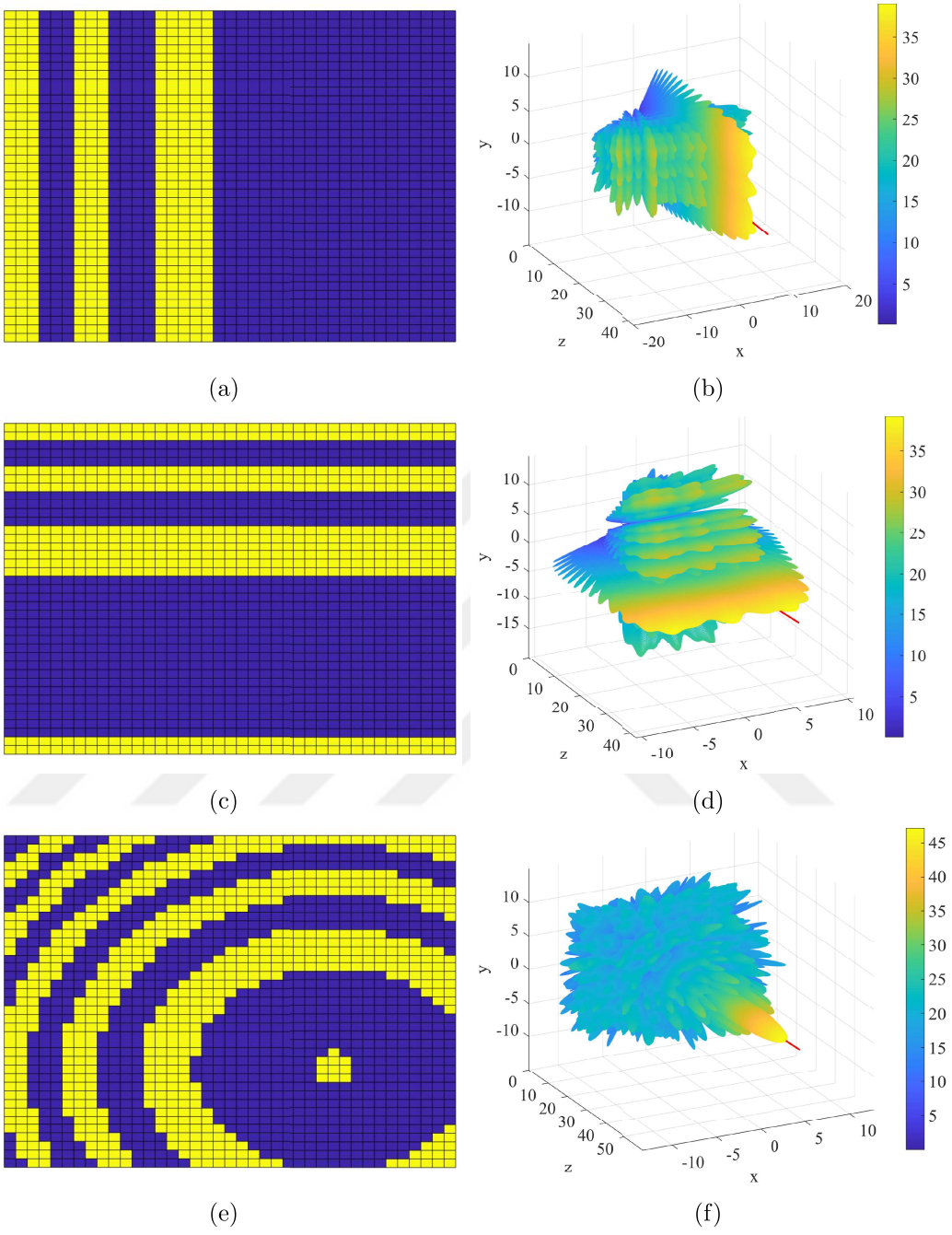

Figure 3.3. Configuration found by searching the optimum configuration for (a) $\varphi = 0^\circ$ beam planes, (b) $\varphi = 90^\circ$ beam planes, and (c) all beam space. (d), (e), and (f) give the radiation patterns of the corresponding configuration.

3.2. CNN Model

CNN is a type of deep learning algorithm commonly used in image and video processing tasks. Unlike traditional neural networks, CNNs are specifically designed to process data with a grid-like topology, such as images, by utilizing a series of convolutional layers to extract relevant features from the input data. Generally, this feature extraction process is followed by one or more fully connected layers, which use the extracted features to perform classification or regression tasks. However, in this study, the CNN is not utilized to perform classification or regression, but to learn the relationship between the input images and the output image in order to generate the RIS configuration (i.e., Figure 3.3 (c)) by using the configurations that optimize the RIS vertically (i.e., Figure 3.3 (a)) and horizontally (i.e., Figure 3.3 (b)). In this figure, the relation between the input configurations and the output configuration can be clearly seen. The idea behind this use is that a given point in 3D space lies on a line that can be expressed in terms of the intersection of two non-parallel planes, and these planes are chosen to be perpendicular to reveal the features clearly. Besides, to reduce complexity, these two perpendicular planes are determined as the horizontal and vertical planes of the RIS.

Table 3.1. The proposed CNN model architecture.

Layer	**Output Shape**	**Filter Shape**
Input	40 x 40 x 2	-
Conv3D_1	40 x 40 x 4	3 x 3 x 2
Conv3D_2	40 x 40 x 16	3 x 3 x 2
Conv3D_3	40 x 40 x 32	3 x 3 x 4
Dropout (0.2)	40 x 40 x 32	-
Conv3D_4	40 x 40 x 128	5 x 5 x 8
Conv3D_5	40 x 40 x 64	5 x 5 x 8
Conv3D_6	40 x 40 x 8	3 x 3 x 4
Dropout (0.2)	40 x 40 x 8	-
Conv3D_7	40 x 40 x 4	3 x 3 x 2
Conv3D_8	40 x 40 x 1	3 x 3 x 2
Output	40 x 40	-
Trainable Parameters	2,496,665	

The open-source machine learning framework Keras [41] is used to develop and design CNN for generating the optimal RIS setup. The proposed CNN model consists of six 3D convolutional layers and two dropout layers. The 3D convolutional layers have 4, 16, 32, 128, 64, 8, 4, and 1 filters, respectively, with kernel sizes of (3 × 3 × 2), (3 × 3 × 2), (3 × 3 × 4), (5 × 5 × 8), (5 × 5 × 8), (5 × 5 × 8), (3 × 3 × 3), (3 × 3 × 2), and (3 × 3× 2), respectively and the hyperbolic tangent (tanh) activation function is used in each convolutional layer. In order for a network to be capable of better generalization and not to over-fit data, the dropout layers are used with a rate of 0.2. Furthermore, the model parameters are chosen using the adaptive moment estimation (ADAM) optimizer, and early stopping is used during the training phase to avoid over-fitting. For the early stopping function, a patience of 10 epochs is set, which checks the validation loss throughout training. If the validation loss converges to a level and stays there for 10 epochs, the training is stopped, and the weights from the final training run are utilized in the test. Table 3.1 and Figure 3.4 provide the implementation design for the suggested CNN model.

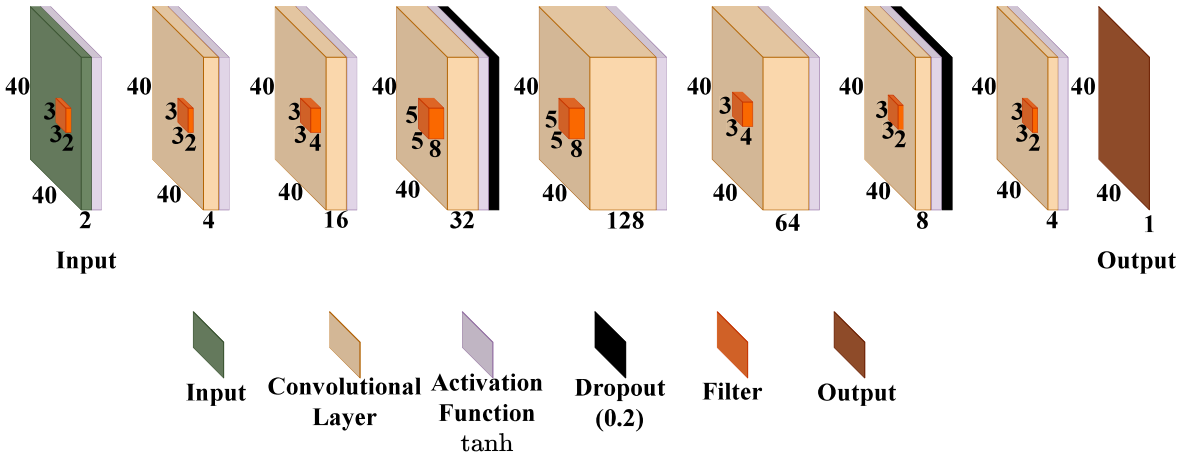

Figure 3.4. The CNN architecture illustration.

3.3. Results of the CNN-Based Optimization Approach

The dataset is generated using the algorithm in Figure 3.2 for input configurations and the algorithm in Figure 3.1 for label configurations for different angular positions of the R_x in such a way that the R_x is located at the far-field of the RIS with azimuth and elevation angles in the range [0°, 180°] and [−60°, 60°], respectively, with step size 1°. Two input images of RIS configurations, including one vertical and one horizontal optimization result, and one output image of RIS configuration for overall optimization result are generated for each position. For the overall optimization, the RIS configuration is found by the iterative method [26] by searching for the best phase state for each element one by one instead of each row or column as in the algorithm in Figure 3.2. For each angular position, three sets of data for training, one set of data for validation, and one set of data for testing are generated. There are slight differences between the configurations generated within the sets as a result of the randomization of the steps taken in the iterative method to ensure generalization during model training.

The model was able to learn final configuration extraction from the inputs for most angles. Even if the generated configuration is not exactly identical to the label, it gives a similar radiation pattern with a peak in the desired direction. An example of the estimated configuration and the corresponding pattern is shown in Figure 3.5.

This configuration is the estimated version of the configuration given in Figure 3.3 (e) where the model uses Figure 3.3 (a) and (c) as input configurations. Since this example shows one position result, to evaluate the general performance of the model, it is tested with all the integer angle combinations in the plane of [0°, 180°] and [−60°, 60°] for azimuth and elevation, respectively. The elevation interval is chosen as is with the assumption that the RIS performance drastically decreases as the elevation angle increases. For comparison, the classical iterative algorithm is used as a reference. At each test, the powers at each angle combination for both algorithms are recorded, and the power of the proposed model is subtracted from the power of the reference algorithm. The result is shown in Figure 3.6.

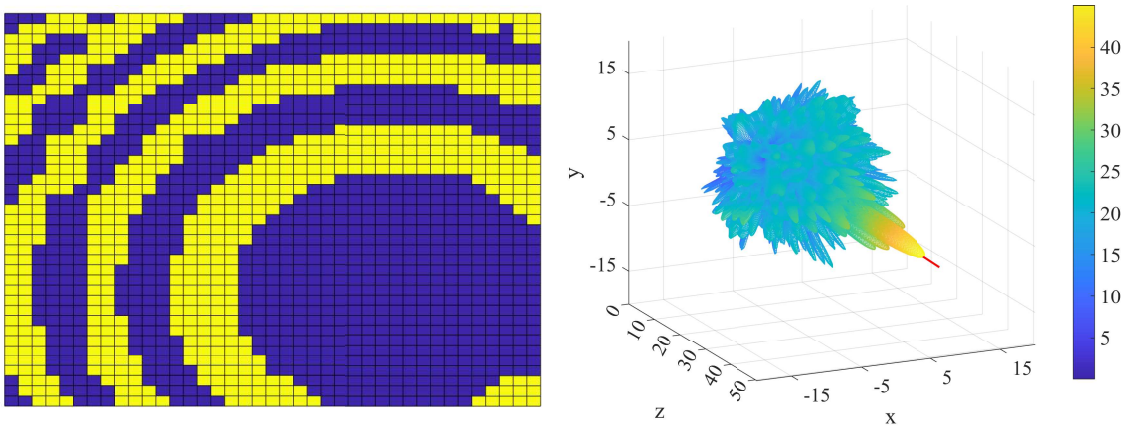

(a) (b)

Figure 3.5. (a) Estimated configuration of the proposed CNN model and (b) the radiation pattern of this configuration.

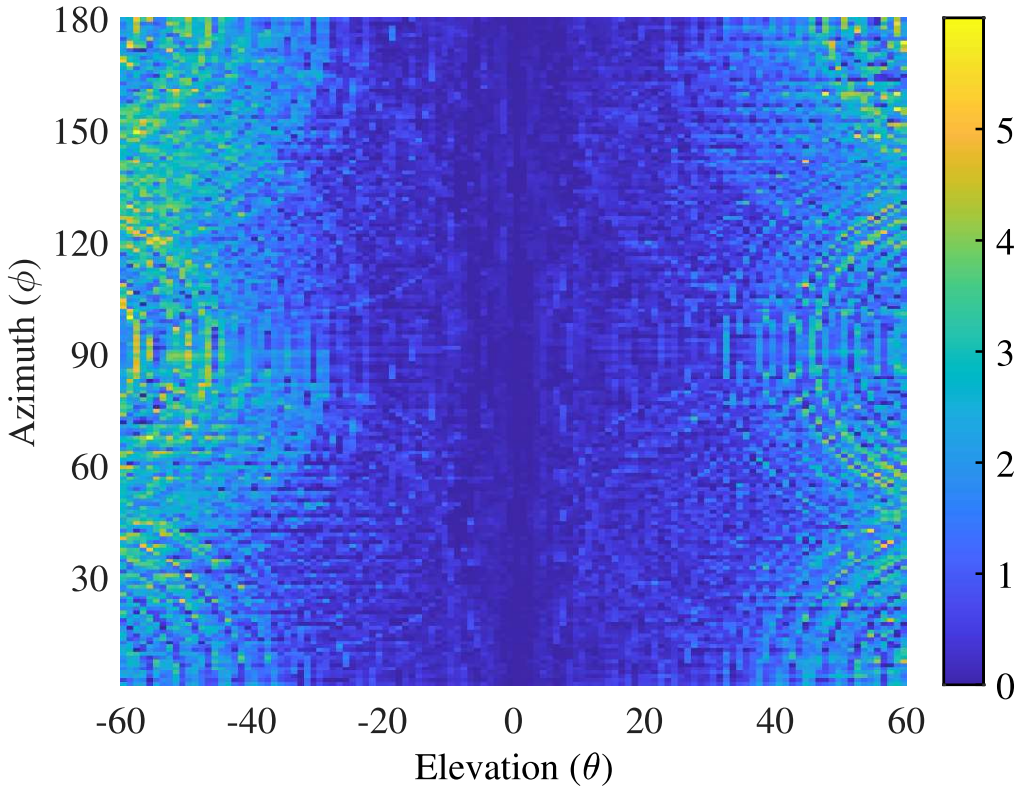

Figure 3.6. The distribution of the power differences between the iterative method and the proposed method over the angular position of the receiver.

It can be observed from the figure that the proposed model gives a close performance to the classical iterative algorithm within at most 5dB. Specifically, performance drops occur in the elevation angles around the edges. Furthermore, for an elevation interval of -45° to 45°, the performance difference is negligible. The reason is that the configurations required to form peaks at edges are more complicated and harder to learn than those for the middle. This is illustrated in Figure 3.7. The configuration of Figure 3.7(a) is learnable and can be estimated by the CNN as in Figure 3.7(b). On the other hand, Figures 3.7(c) and (d) show a sophisticated configuration and its coarse estimation by the CNN, respectively.

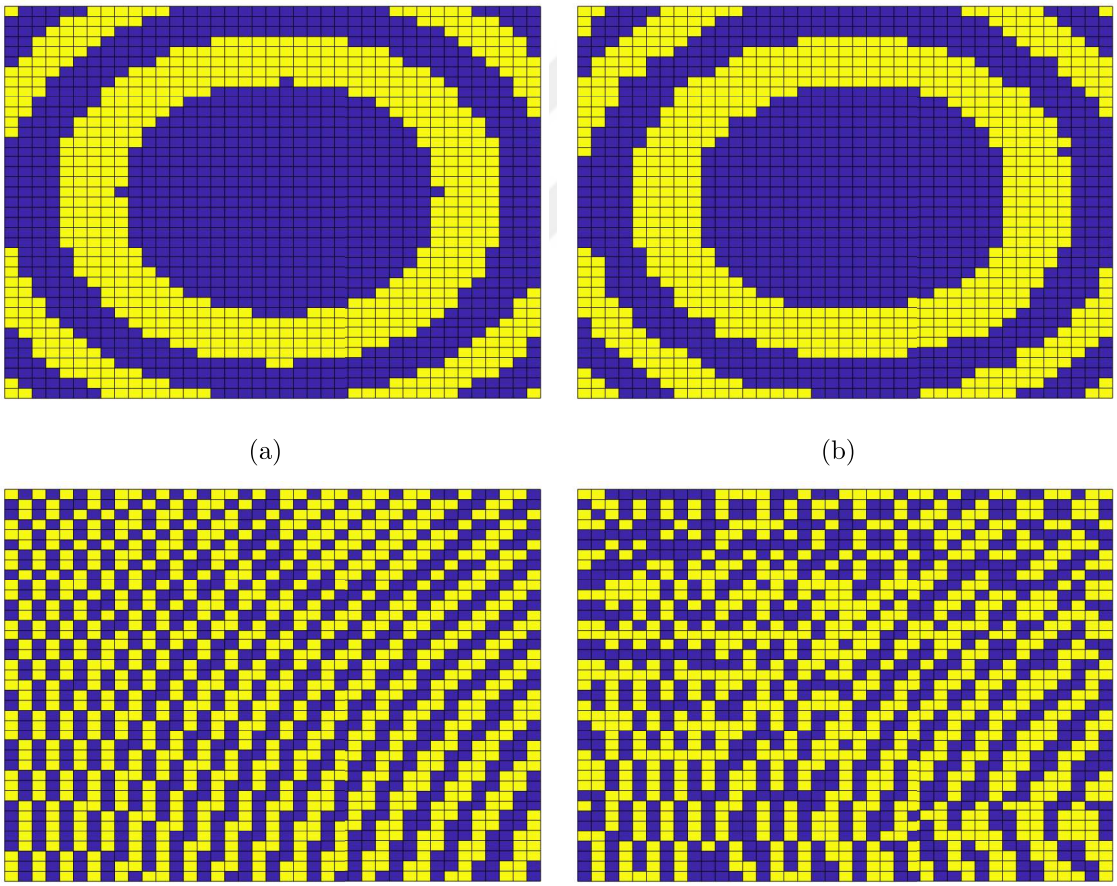

(a) (b)

(c) (d)

Figure 3.7. The illustration of the real configurations ((a), (c)) and their estimated configurations ((b), (d)) for $\vartheta = 0^\circ, \varphi = 0^\circ$ and $\vartheta = 60^\circ, \varphi = 300^\circ$, respectively.

Apart from these, to visualize the performance of the CNN model, the comparison of the received power of the method given in [29] with the received power of the same reference algorithm is illustrated in Figure 3.8. In [29], the configuration is found by deciding the horizontal configuration as in the algorithm in Figure 3.2 but then deciding the vertical configuration by keeping the horizontal configuration active on the RIS. The decrease in performance is also observable as the elevation angles approach the edges.

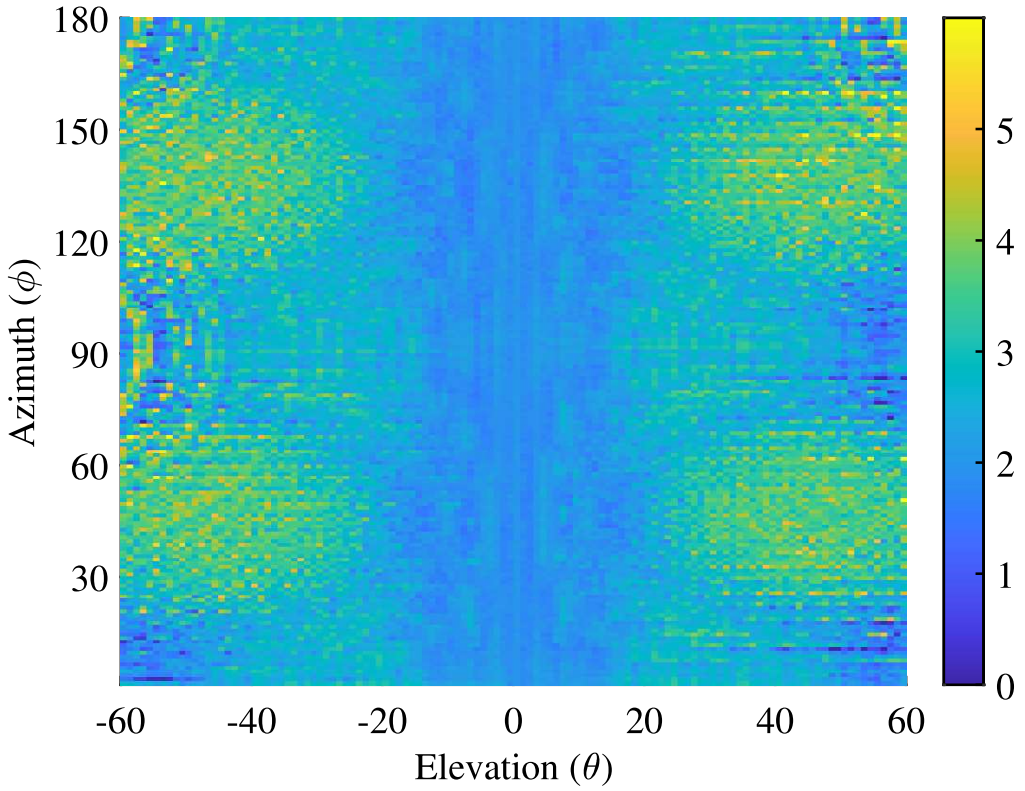

Figure 3.8. The distribution of the power differences between the iterative method and the horizontal and vertical stripe grouping method over the angular position of the receiver.

When the results in Figure 3.6 and Figure 3.8, the proposed CNN model decreases the received power differences with the reference algorithm in general. According to [29], the resulting configuration and its radiation pattern for one location are given in Figure 3.9. As can be seen, although the maximum gain of the radiation pattern

exists in the direction of the receiver, the efficiency loss is obvious due to horizontal and vertical beam planes. The model makes the resulting configuration to be smoother than the configuration generated by [29] seen in Figure 3.9 (a), which suppresses the radiated power existing in the non-interested part of the horizontal and vertical beam planes that can be seen from Figure 3.9 (b).

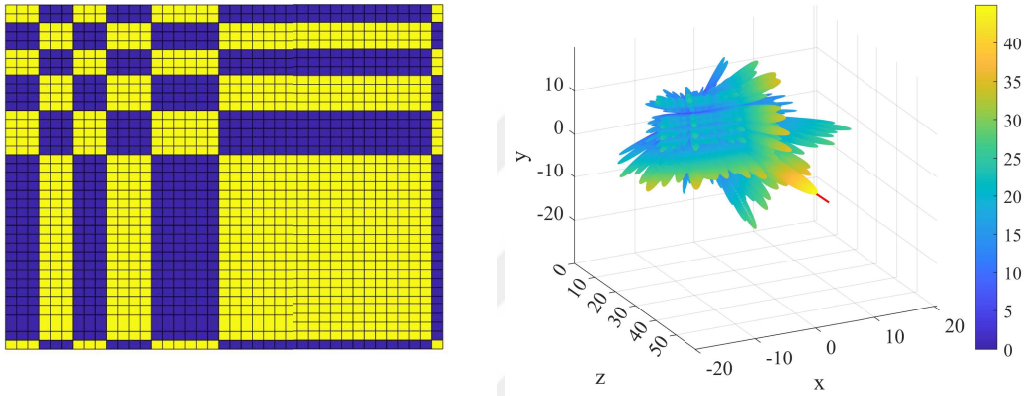

(a) (b)

Figure 3.9. (a) The configuration found according to the algorithm given in [29] and (b) the radiation pattern of this configuration.

4. COVERAGE OPTIMIZATION IN THE PRESENCE OF ANOTHER USER

In this chapter, the coverage optimization in the presence of another user will be examined. In the first section, the simultaneous coverage enhancement of both users will be analyzed under two constraints: a) fair gain distributions and b) prioritized gain distributions. After that, the coverage enhancement of one user by mitigating the interference to another user will be investigated under two conditions: a) maximizing the power differences and b) maximizing the power differences considering the interference minimization with a threshold level. In this chapter, the RIS is modeled with 76 elements in 8 rows and 10 columns. A real prototype of the RIS [42] is utilized in the measurement part of the coverage enhancement with interference mitigation which will be explained in Section 4.2. In this prototype, there is a controller part on the bottom left corner of the RIS, where there are no antenna cells. Hence the RIS used in the simulations is modeled in that way. Although there are no measurement results provided for other sections, for the sake of consistency, the RIS is modeled as explained for all the sections in this chapter.

4.1. Simultaneous Coverage Enhancement of Both Users

In this section, concurrent coverage enhancement, one of the approaches explained in Section 2.2, will be analyzed. First, the fair coverage enhancement of both users will be investigated by explaining the utilized algorithm and resulting configurations with their corresponding radiation patterns. After that, the prioritized coverage enhancement will be examined in the same way.

4.1.1. Fair Coverage Enhancement of Both Users

When the aim is to increase the received powers of two users equitably, the objective of the problem given in (2.13) can be rewritten as

$$\begin{aligned} \boldsymbol{\Theta}^* = \arg\max_{\phi_{mn}} \frac{P_{rx_1} P_{rx_2}}{P_{rx_1} + P_{rx_2}} \\ \text{s.t. } \phi_{mn} \in \{0^\circ, 180^\circ\}, \quad \forall mn, \end{aligned} \tag{4.1}$$

where P_{rx_1} and P_{rx_2} are defined in (2.12) in terms of the phases of the RIS. The geometric mean is chosen as the received power maximization method, since the purpose is to enhance the received powers of the receivers while minimizing the difference between them [43].

Analytically solving the current problem is not a straightforward task because the RIS is a passive device and there are no RF chains behind the antenna cells which would be utilized to channel estimations. Therefore, the modified version of the algorithm given in Figure 3.1 can be used to solve this problem, which is summarized in the algorithm given in Figure 4.1.

Input: P_{rx_1}, P_{rx_2}, M, N, and P
Output: $\boldsymbol{\Theta}$ (The phase shift values of the RIS elements)
1: initialize $\boldsymbol{\Theta}$ with 0° phase shift
2: $P_{joint}^{max} \leftarrow -\infty$
3: **for** $i \in [1, M \times N]$ **do**
4: **for** $j \in [1, P]$ **do**
5: configure ith diagonal element of $\boldsymbol{\Theta}$ with jth phase shift
6: measure P_{rx_1} and P_{rx_2}
7: calculate P_{joint} (according to (2.13) or (4.2))
8: **if** $(P_{joint} > P_{joint}^{max})$ **then**
9: update ith diagonal element of $\boldsymbol{\Theta}$ with jth phase shift
10: $P_{joint}^{max} \leftarrow P_{joint}$
11: **end if**
12: **end for**
13: **end for**
14: **return** $\boldsymbol{\Theta}$

Figure 4.1. The modified iterative algorithm for coverage optimization for two-user through RIS.

According to this iterative algorithm, all the phase delays of the RIS are set to 0° first. Subsequently, the RIS controller utilizes received power feedback from the two receivers to iteratively determine the phase delay of each cell by evaluating the joint power according to (4.1) and comparing it with the maximum joint power obtained up to the current iteration. Keeping the phase delay determined for each antenna cell, the procedure is applied for the next cell and continues until the phase delay of the last cell of the RIS is determined. Finally, the resulting phase delays provide the optimal RIS configuration.

4.1.2. Prioritized Coverage Enhancement of Both Users

When the aim is to increase the received powers by prioritizing one of the users, the objective of the problem given in (2.13) can be revised as

$$\begin{aligned} \boldsymbol{\Theta}^* = \arg\max_{\phi_{mn}} \frac{w_1 P_{rx_1} + w_2 P_{rx_2}}{w_1 + w_2} \\ \text{s.t. } \phi_{mn} \in \{0°, 180°\}, \quad \forall mn, \end{aligned} \tag{4.2}$$

where P_{rx_1} and P_{rx_2} are defined in (2.12) in terms of the phases of the RIS and w_1 and w_2 are the weights that are used to determine the prioritization of the users. The well-known weighted average [44] is used to define the received powers in terms of prioritization.

With the same reasoning explained in Subsection 4.1.1, it is difficult to approach this problem analytically. Therefore, the algorithm given in Figure 4.1 can be used by calculating the joint power term according to (4.2). The rest of the algorithm is the same as the one given in Subsection 4.1.1.

4.1.3. Results of Simultaneous Coverage Enhancement of Both Users

In this subsection, the simulation results of the simultaneous coverage optimization for a two-user scenario will be discussed under two categories: a) Fair Coverage Enhancement and b) Prioritized Coverage Enhancement. The simulation environment

is set up on the MATLAB R2022a platform. The RIS in the simulations is a 1-bit RIS composed of 76 elements. This RIS configuration is chosen like that because there is a prototype with these specifications and it is used for the verification of some simulations. The RIS is placed at the origin and the transmitter and receivers are located in front of the RIS in a way that the transmitter is on the near field and the receivers are on the far field of the RIS [45] as can be seen in Figure 2.2. The angular position of the transmitter is $(2m, 10°, 100°)$ in the order of range, elevation, and azimuth angles. In the same order, the positions of Rx_1 and Rx_2 are $(10m, 20°, 45°)$ and $(10m, 10°, 210°)$, respectively. For the simulations, the gain of the RIS is calculated for all the directions having elevation angles between $[-60°, 60°]$ and azimuth angles between $[0°, 180°]$. Besides, the changes in the received power of the receivers through the iterations are also saved.

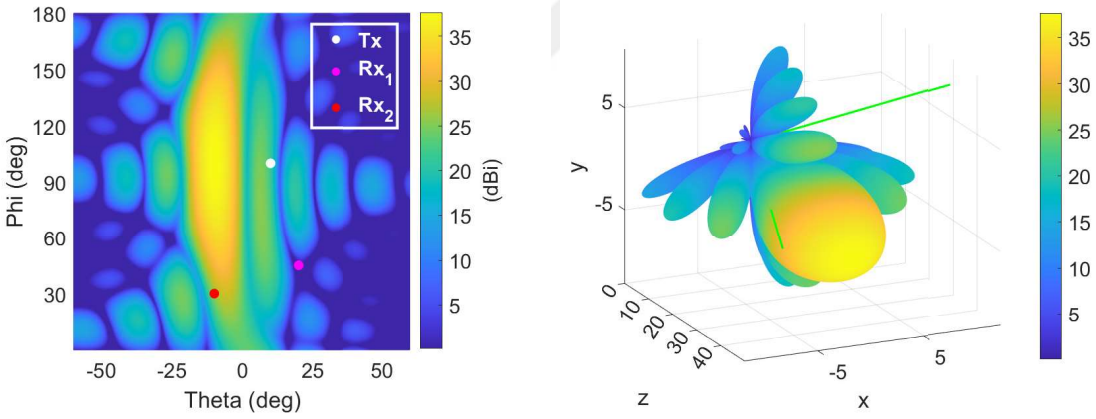

(a) (b)

Figure 4.2. Scattered radiation pattern of the RIS before any phase optimization (a) in terms of azimuth and elevation angles and (b) in terms of cartesian coordinates.

Before presenting the results for fair and prioritized RIS gain distributions, the results of the radiation pattern before any optimization are provided as a reference in Figure 4.2 in which (a) represents the radiation pattern with respect to azimuth and elevation angles and (b) represents the 3D radiation in cartesian coordinates. In Figure 4.2 (a), the white dot represents the angular position of the transmitter while red and magenta dots represents the receivers' angular positions. The green lines in Fig 4.2 (b)

represents the directions of the receivers. As can be understood from this figure, before any optimization and when all the phase delays of the RIS are set as 0°, the radiation is oriented symmetrically to the transmitter with respect to the origin. The RIS gains toward Rx_1 and Rx_2 are -4.1 dB and 25.9 dB, respectively.

To evaluate the effect of the presence of another user while coverage optimization, the results of the coverage optimization considering only one receiver are provided. The received power levels of the receivers with respect to iterations, when the objective is to optimize the coverage for only Rx_1, are provided with the resulting configuration in Figure 4.3. As the received power of the Rx_1 increases, the received power of the Rx_2 decreases even if there is no intention to decrease it. When Figure 4.2 and Figure 4.4 are examined together, it is clearly seen that the reflection from the RIS before the optimization is towards around the Rx_2, and with the optimization, the RIS reflection starts to focus on Rx_1 causing the received power of Rx_2 to decrease.

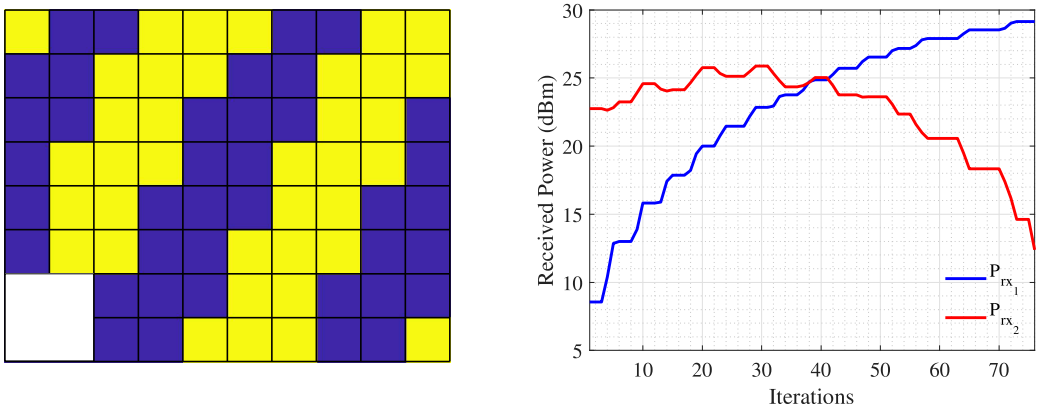

(a) (b)

Figure 4.3. When the coverage optimization is applied by considering only the first receiver, (a) resulting configuration of the RIS (b) the received power levels with respect to iterations.

The lower left corner of the configuration, seen as a white rectangle, corresponds to the RIS's controller which is because of the RIS prototype mentioned at the beginning of the chapter. As can be seen from Figure 4.3, there exists a pattern in the

configuration for generating directivity to a specific angle. When it is compared with the configurations in Chapter 3, the lack of the number of elements of the RIS causes the pattern to be incomplete, which in return results in the undesired directivity lobe existing illustrated in Figure 4.4.

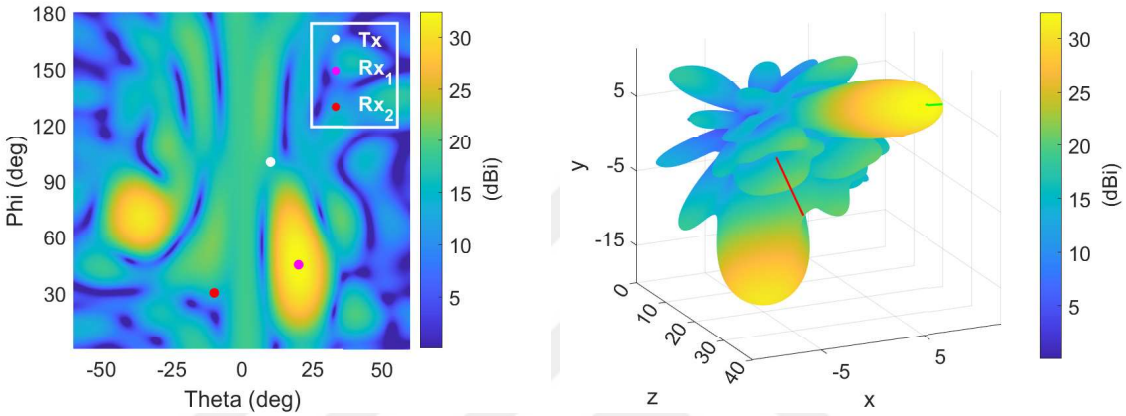

Figure 4.4. Scattered radiation pattern of the RIS when the coverage optimization is applied by considering only the first receiver (a) in terms of azimuth and elevation angles and (b) in terms of cartesian coordinates.

4.1.3.1. Results of Fair Power Distribution. The results of the fair gain distributions of the RIS are illustrated in Figure 4.5 and Figure 4.6. In Figure 4.5, it is seen that the first half of the iterations are utilized to increase the gain in the direction of Rx_1, and the configurations and power changes with respect to iterations are similar to ones given in Figure 4.3 for the first half of the iterations. On the other hand, the last half of the iterations are utilized to prevent the gain in the direction of Rx_2 to drop, which enables the gain levels to be close to each other.

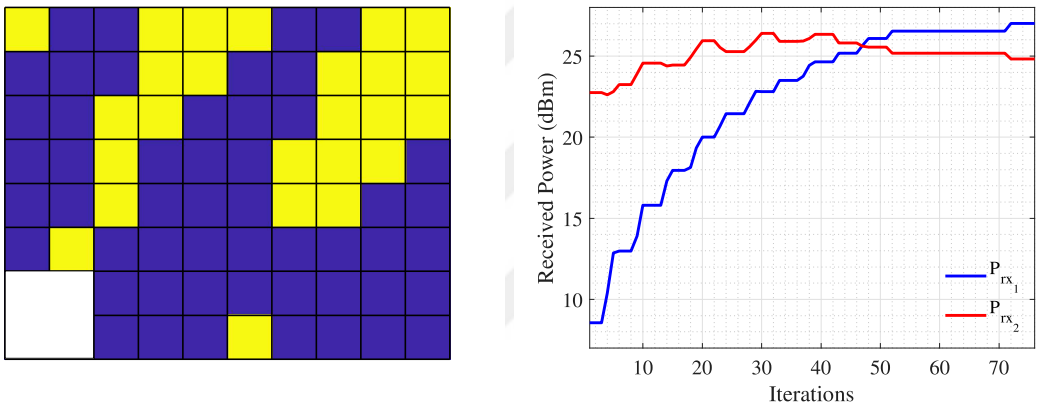

(a) (b)

Figure 4.5. When the coverage optimization is applied by considering the receivers in a fair way, (a) resulting configuration of the RIS (b) the received power levels with respect to iterations.

It can be seen from the colors in Fig 4.6 that the RIS gain is divided in a way that the coverage is enhanced for both users fairly. The gains of the RIS for the receivers are 29.9 dB and 30.2 dB for Rx_1 and Rx_2, respectively. As in Figure 4.4, it is seen that an undesired beam is formed in Figure 4.6 as well. As explained before, the reason behind this phenomenon is the insufficient number of RIS elements. Besides, when the gain levels are compared with Figure 4.4, it is seen that the gain levels of fair distribution are lower than the one that exists in the one user optimization case, which is an expected outcome because of the gain capacity of the RIS is divided for two receivers.

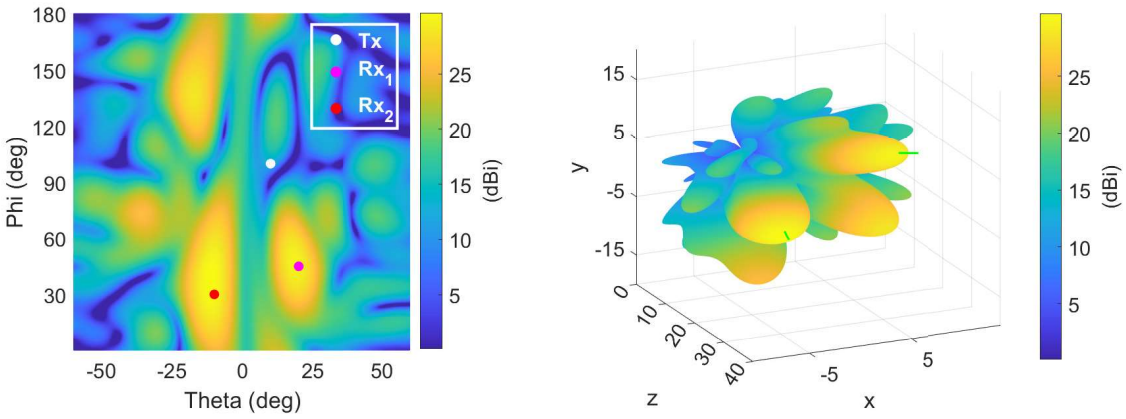

Figure 4.6. Scattered radiation pattern of the RIS after the fair coverage optimization for two receivers (a) in terms of azimuth and elevation angles and (b) in terms of cartesian coordinates.

4.1.3.2. Results of Prioritized Power Distribution. The results for the prioritized gain distribution of the RIS are illustrated in Figure 4.7 and Figure 4.8. The first two rows of the configuration given in Figure 4.7 (a) are exactly the same as the first two rows of the resulting configuration for fair gain distribution, making it have the same power variation profile as the fair distribution power variation profile for the first steps of optimization. As can be seen from Figure 4.7 (b), the received powers of the receivers increase with the iterations, however, there is a difference between the power levels of the receivers stemming from the prioritization. When compared with the ones in Figure 4.5, an increase in the received power for one user causes more degradation in the received power of the other user. The weights are defined as $w_1 = 0.33$ and $w_2 = 0.67$ for Rx_1 and Rx_2, respectively. Hence, Rx_2 is determined as the prioritized user in this scenario. While the received power of Rx_1 increases from 8.6 dBm to 23.7 dBm, the power of Rx_2 increases from 22.7 dBm to 27.4 dBm.

As can be seen from Figure 4.8, the RIS gain is distributed over the non-interested regions. The difference in the RIS gain levels is obvious but the coverage is still enhanced for the user with lower gain. The gains of the RIS for Rx_1 and Rx_2 directions

become 27.6 dB and 30.4 dB, respectively.

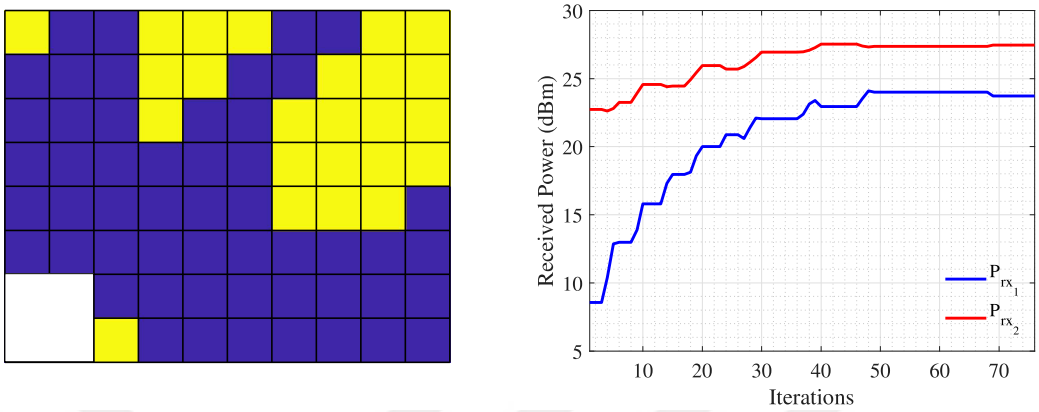

(a) (b)

Figure 4.7. When the coverage optimization is applied by considering the receivers by prioritizing Rx_2, (a) resulting configuration of the RIS (b) the received power levels with respect to iterations.

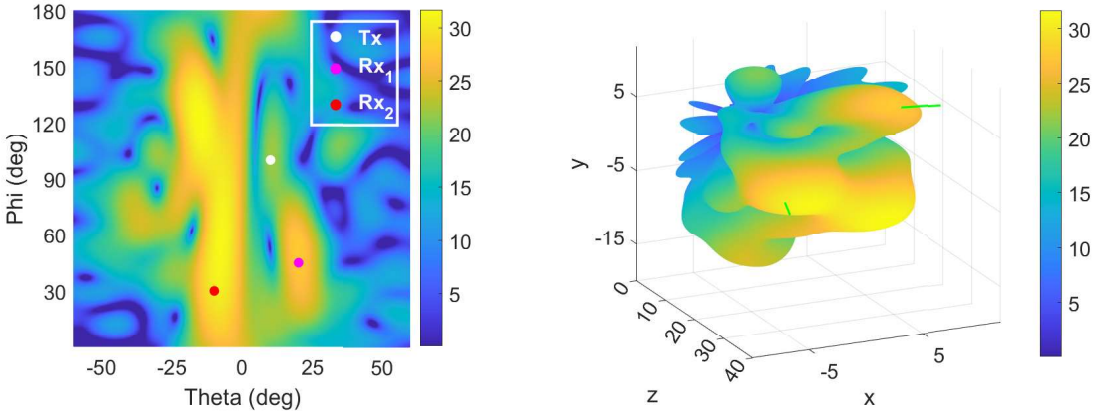

(a) (b)

Figure 4.8. Scattered radiation pattern of the RIS after the prioritized coverage optimization for two receivers (a) in terms of azimuth and elevation angles and (b) in terms of cartesian coordinates.

4.2. Coverage Enhancement of One User by Mitigating The Interference for Other

In this section, increasing one user's coverage while reducing other users' interference via RIS will be investigated. The RIS utilization in this concept will be investigated under two categories. First, the objective is to increase the power ratio as much as possible. Second, the objective is to increase the power ratio of the receivers until the received power of the unintended receiver decrease under a threshold level and then to increase the received power of the intended user. Actually, this phenomenon is known as the PLS in the literature. Hence, throughout the section, the Rx_1, which is the intended user, is called Bob and the Rx_2, which is the unintended user, is called Eve and the transmitter is called Alice for consistency with the PLS literature.

4.2.1. Optimal Secrecy Capacity Maximization

When the aim is to increase the ratio of the received powers of Bob and Eve, the objective of the problem given in (2.13) can be rewritten as

$$\begin{aligned} \boldsymbol{\Theta}^* = \arg\max_{\phi_{mn}} \frac{P_b}{P_e} \\ \text{s.t. } \phi_{mn} \in \{0^\circ, 180^\circ\}, \quad \forall mn, \end{aligned} \tag{4.3}$$

where P_b and P_e are the received power of Bob and Eve, respectively and they are calculated as P_{rx1} and P_{rx2} defined in (2.12) in terms of the phases of the RIS.

When the term $\frac{P_b}{P_e}$ is rewritten as

$$\begin{aligned} \frac{P_b}{P_e} &= \frac{S_b + N_b}{S_e + N_e} \\ &= \frac{1 + \frac{S_b}{N_b}}{1 + \frac{S_e}{N_e}} \frac{N_b}{N_e}, \end{aligned} \tag{4.4}$$

Since logarithm is a monotonically increasing function, maximizing a variable is equivalent to maximizing the logarithm of this variable. Then taking the logarithm of both sides gives

$$\begin{aligned}\log_2\left(\frac{P_b}{P_e}\right) &= \log_2\left(\frac{1+\frac{S_b}{N_b}\frac{N_b}{N_e}}{1+\frac{S_e}{N_e}}\right), \\ &= \log_2\left(1+\frac{S_b}{N_b}\right) - \log_2\left(1+\frac{S_e}{N_e}\right) + log_2(N_b) - log_2(N_e) \\ &= C_b - C_e + log_2(N_b) - log_2(N_e),\end{aligned} \tag{4.5}$$

where $(S_b,\ N_b)$ and $(S_e,\ N_e)$ are the signal and noise powers pairs at Bob and Eve, respectively, and C_b and C_e are the capacities for Bob and Eve, respectively. If the noise powers are accepted as the same for Bob and Eve, (4.5) is simplified as

$$\log_2\left(\frac{P_b}{P_e}\right) = C_b - C_e = C_s, \tag{4.6}$$

where C_s is the secrecy capacity of Bob and Eve. Note that the secrecy capacity cannot be negative but for the RIS to be optimized, the C_s term is accepted to have negative values. Then, the objective of the RIS in (4.3) can be replaced with C_s.

When the received power calculations given in (2.12) are considered, even if all the channel information is available, it is quite complicated to calculate $\mathbf{\Theta}$ maximizing C_s theoretically. Therefore, the received signal powers can be directly used as in (4.6) to calculate C_s. Then, the maximum secrecy capacity can be obtained as

$$\begin{aligned}\mathbf{\Theta}^* = \arg \max_{\phi_{mn},\forall mn}\ & C_s \\ \text{s.t. } & \phi_{mn} \in \{0^\circ, 180^\circ\}, \quad \forall mn.\end{aligned} \tag{4.7}$$

Since an exhaustive search is impractical, the algorithm in Figure 4.9, inspired from [26], is utilized to determine the RIS configuration. $\mathbf{\Theta}$ is a vector including the phase shifts of the RIS elements initially configured as 0°. Each element has one state, which can be any of P distinct values. The algorithm applies P specific phase shifts to each element, chosen randomly and only once. The corresponding part of $\mathbf{\Theta}$ is updated using the phase shift of the selected element that maximizes C_s between Bob and Eve. The exact process is sequentially performed for each remaining element until all the elements are considered. Finally, the algorithm returns $\mathbf{\Theta}$ as the RIS configuration aiming to maximize the secrecy capacity.

Input: P_b, P_e, M, N, and P
Output: $\mathbf{\Theta}$ (The phase shift values of the RIS elements)
initialize $\mathbf{\Theta}$ with 0° phase shift
$C_s^{max} \leftarrow -\infty$
$Steps \leftarrow$ shuffle $[1, M \times N]$
for $i \in Steps$ **do**
  for $j \in [1, P]$ **do**
    configure ith diagonal element of $\mathbf{\Theta}$ with jth phase shift
    calculate P_b and P_e
    calculate C_s (according to (4.6))
    if $(C_s > C_s^{max})$ **then**
      update ith diagonal element of $\mathbf{\Theta}$ with jth phase shift
      $C_s^{max} \leftarrow C_s$
    end if
  end for
end for
return $\mathbf{\Theta}$

Figure 4.9. The modified iterative algorithm for secrecy capacity maximization.

4.2.2. Sub-optimal Secrecy Capacity Maximization

In this subsection, the aim is to increase the ratio of the received powers of Bob and Eve until the received power of Eve is held under a threshold, then the goal becomes to increase the received power level of Bob. If Eve's received power rises above the threshold, the aim becomes to increase the ratio of the received powers again. Hence, the objective of the problem given in (2.13) can be rewritten as

$$\mathbf{\Theta}^* = \arg\max_{\phi_{mn}} \begin{cases} \frac{P_b}{P_e}, & \text{if } P_e \geq threshold \\ P_b, & \text{otherwise} \end{cases} \tag{4.8}$$
$$\text{s.t. } \phi_{mn} \in \{0^\circ, 180^\circ\}, \quad \forall mn,$$

where P_b and P_e are the received power of Bob and Eve, respectively and they are calculated as P_{rx1} and P_{rx2} defined in (2.12) in terms of the phases of the RIS. The threshold value is defined according to the requirement defined for tolerable interference power for Eve. The goal of using such an objective is to utilize RIS for coverage enhancement for Bob after ensuring the interference reduction for Eve to a predefined

extent. Hence, the RIS gain in the direction of Bob increases with the trade-off by decreasing the interference less.

Input: P_b, P_e, M, N, and P
Output: $\mathbf{\Theta}$ (The phase shift values of the RIS elements)
initialize $\mathbf{\Theta}$ with 0° phase shift
$C_s^* \leftarrow -\infty$, $P_b^* \leftarrow -\infty$
Steps $\leftarrow$ shuffle $[1, M \times N]$
for $i \in$ *Steps* **do**
  for $j \in [1, P]$ **do**
    configure ith diagonal element of $\mathbf{\Theta}$ with jth phase shift
    calculate P_b and P_e
    calculate C_s (according to (4.6))
    if $P_e >$ *threshold* **then**
      if $(C_s > C_s^*)$ **then**
        update ith diagonal element of $\mathbf{\Theta}$ with jth phase shift
        $C_s^* \leftarrow C_s$, $P_b^* \leftarrow P_b$
      end if
    else
      if $(P_b > P_b^*)$ **then**
        update ith diagonal element of $\mathbf{\Theta}$ with jth phase shift
        $C_s^* \leftarrow C_s$, $P_b^* \leftarrow P_b$
      end if
    end if
  end for
end for
return $\mathbf{\Theta}$

Figure 4.10. The modified iterative algorithm for secrecy capacity maximization with thresholding method.

The modified version of the algorithm in Figure 4.9 is used for the optimization of the RIS for this objective. The pseudocode is given in the algorithm in Figure 4.10 where $\mathbf{\Theta}$ is a vector including the phase shifts of the RIS elements initially configured as 0°. Each element has one state, which can be any of P distinct values. For each distinct phase value, the received powers of Bob and Eve are calculated and the secrecy capacity between them is calculated also. The *threshold* value is defined before the optimization and the received power of Eve falling under the threshold level turns the objective into maximizing Bob's received power. Finally, the terms $\mathbf{\Theta}$ is determined

to maximize the objective given in (4.8).

4.2.3. Results of Coverage Optimization and Interference Minimization Simultaneously

In this subsection, the simulation results of the coverage enhancement of one user by mitigating the gain for the other user scenario will be discussed under two categories. The simulation environment is generated in MATLAB R2022a according to the system model in Figure 2.1, where the RIS is placed at the origin. Alice, Bob, and Eve are located in the simulation region of $10m \times 10m \times 10m$ such that Alice is in the near field of the RIS while both Bob and Eve are in the far field [45]. The angular position of the Alice is $(2m, 10°, 100°)$ in the order of range, elevation, and azimuth angles. In the same order, the positions of Bob and Eve are $(10m, 20°, 45°)$ and $(10m, 10°, 210°)$, respectively. For the simulations, the gain of the RIS is calculated for all the directions having elevation angles between $[-60°, 60°]$ and azimuth angles between $[0°, 180°]$. Besides, the changes in the received power of the receivers through the iterations are also saved. The RIS prototype used for the measurement experiments consists of 76 elements. Therefore, the simulation scenario includes the RIS having 76 elements such that $M = 8$ and $N = 10$ based on the equations in Section 2.2. Note that the controller part of the RIS having 4 antenna-free cells again will be illustrated with a white rectangle. Furthermore, all the units are located on the front side of the RIS because the RIS is reflecting but not permeable. The algorithms in Figure 4.9 and Figure 4.10 are implemented for the performance evaluation of PLS.

4.2.3.1. Results for Optimal Secrecy Capacity Maximization. A set of computer simulations is performed to demonstrate the impact of the RIS configuration on the received powers of Bob and Eve, where the algorithm in Figure 4.9 is used for configuring the RIS elements. Before beginning the PLS results, for the comparison with the before the optimization situation, Figure 4.2 can be used. In Figure 4.11, the scattered radiation pattern of the RIS is illustrated after the optimization in the form of 2D and 3D. When 4.11 (a), is compared with Figure 4.2 (a), it is clearly seen that the RIS gain is directed

to Bob, and the gain toward Eve is decreased drastically. After the optimization, the RIS gain levels for Bob and Eve become 28.2 dB and 12.2 dB, respectively.

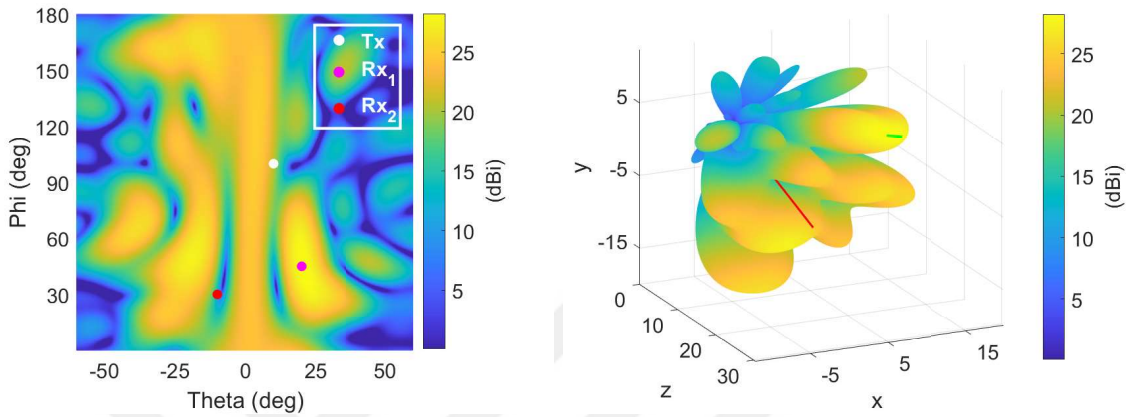

Figure 4.11. Scattered radiation pattern of the RIS after the coverage optimization with interference minimization (a) in terms of azimuth and elevation angles and (b) in terms of cartesian coordinates.

Figure 4.12 illustrates (a) the resulting configuration of the RIS after the optimization and (b) the power changes with respect to iterations. The configuration is somehow similar to the configuration that exists when the RIS is configured according to Rx_1 only case. Examining Figure 4.12 (b) and Figure 4.3 (b) together shows that the power changes are also similar up to a certain iteration. After around iteration 45, the effect of Eve's power becomes evident in the optimization, which stagnates the increase of the received power of Bob. The received powers of Bob and Eve become 25.2 dBm and -5.6 dBm, respectively.

Approximately 1000 simulations of a practical scenario where Alice is in the near-field of the RIS and both Bob and Eve are in the far-field of the RIS, are conducted in a way that the order of elements in *Steps* is randomly chosen for each simulation. The statistics of the received signal powers for Bob and Eve are illustrated in Figure 4.13, where the mean value at each iteration is shown as a dashed line. Furthermore, the boxplot shows the minimum, maximum, median, and first and third quartiles of

the received signal powers. The results demonstrate that the received power of Bob increases from 33 dBm to 42 dBm while the received power of Eve decreases from 30 dBm to 0 dBm on the average through the iterations and therefore, the secrecy capacity significantly increases.

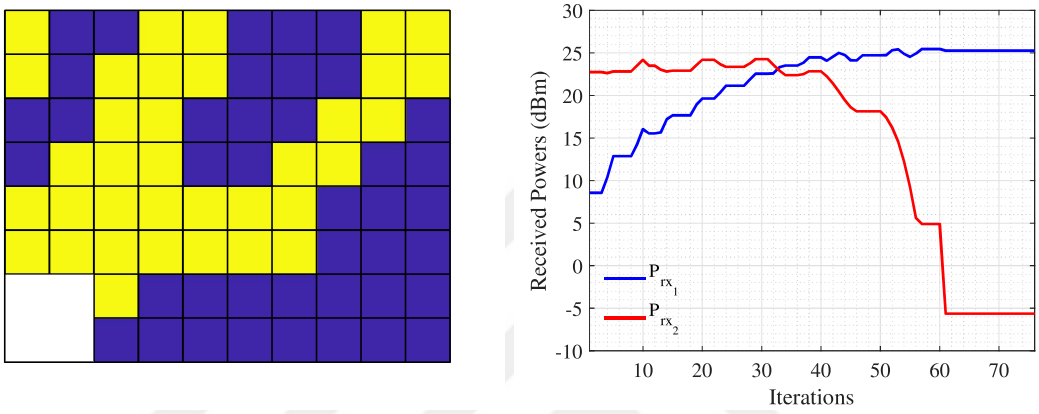

(a) (b)

Figure 4.12. When the coverage optimization is applied by considering maximization of the secrecy capacity, (a) resulting configuration of the RIS (b) the received power levels with respect to iterations.

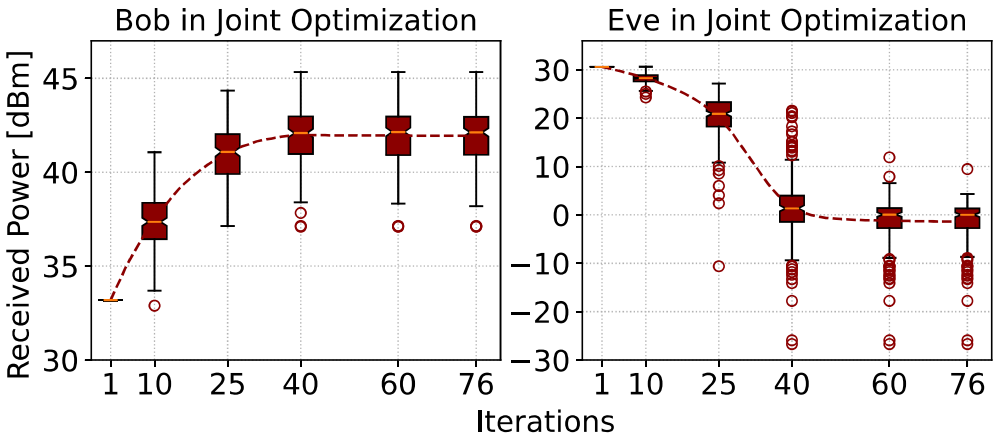

Figure 4.13. Simulation results of the received powers when the objective is to maximize the secrecy capacity.

Figure 4.14 (a) shows that the received signal power of Bob increases from 33 dBm to 48 dBm when the objective is set to maximize the received power of Bob only without considering the received power of Eve. Figure 4.14 (b) illustrates that the received signal power of Eve decreases from 30 dBm to 0 dBm when the objective is set to minimize the received power of Eve only. Note that the received power of Eve fluctuates in both cases and therefore, this phenomenon causes fluctuations in Bob's received power as well when the objective is to maximize the secrecy capacity.

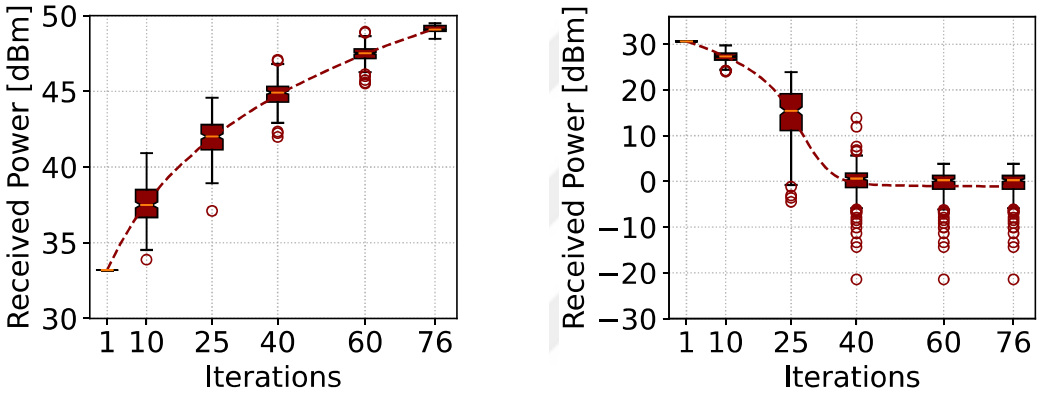

(a) (b)

Figure 4.14. Simulation results of received power of (a) Bob when the objective is to maximize the received power, (b) Eve when the objective is to minimize the received power.

Using ADALM-PLUTO software-defined radio (SDR) modules to transmit and receive over-the-air signals, the RIS-aided wireless communication system is built in an indoor office environment for the measurement of the PLS via the RIS. The measurement setup is shown in Figure 4.15. As seen in Figure 4.15, Alice is positioned in front of the RIS, which is attached to the wall, and Bob and Eve are placed farther away from the RIS.

Using software-controlled phase shifts, the Greenerwave RIS prototype [42] directs the beam from Alice to Bob while eliminating the beam against Eve. The RIS prototype consists of a uniform planar array form with 8×10 reflecting elements, but because the

controller needs a space in the bottom left corner of the 2×2 area, there are actually 76 elements in all. With two PIN diodes corresponding to the horizontal and vertical polarizations, the phase shift of each reflecting element can be independently controlled as 0° or 180°, resulting in four different states.

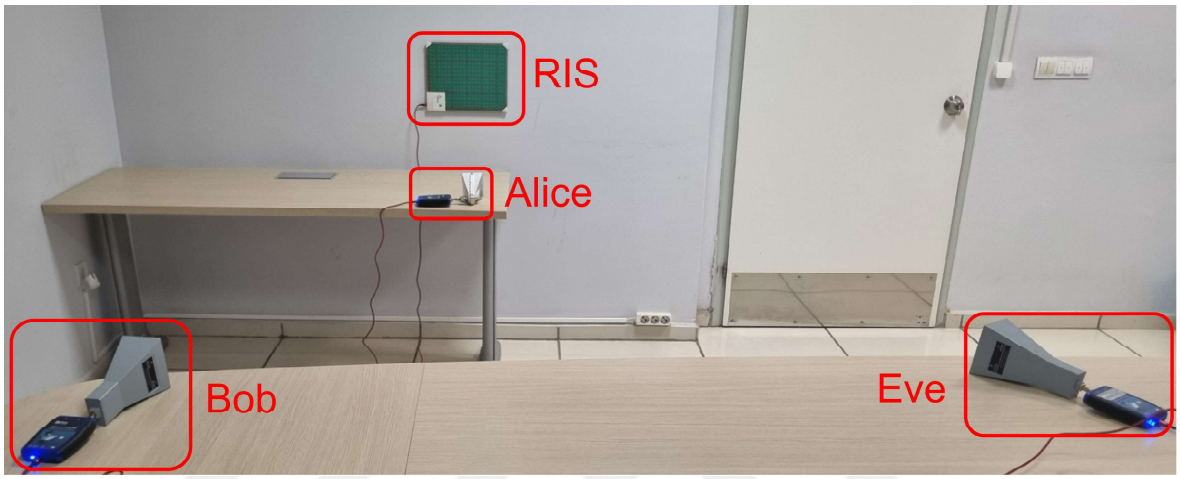

Figure 4.15. The measurement setup of the RIS-assisted wireless communication system.

A Boolean array of 152 elements, which correspond to PIN diodes, is used by a Python script to control the RIS during the measurement campaign, where 0 and 1 represent the phase shifts of 0° and 180°, respectively. The number of time samples required to calculate the average received signal power for both Bob and Eve is chosen to be 100000, and the sampling rate of the terminal SDRs is set to 1 MHz. The reflected signal from the RIS reaches Bob and Eve's horn antennas after Alice transmits a single-tone sinusoidal signal with 100 kHz bandwidth at 5.2 GHz center frequency using a horn antenna facing the RIS. Afterward, each SDR captures the incoming signal and transforms it into complex baseband. Since the SDR has a 12-bit analog-to-digital (ADC) converter, the obtained complex baseband samples are represented by integers in the range of $(-2047, 2048]$. Therefore, the decibels relative to full scale (dBFS) calculation of the average power of the sampled received signal $y_{rx}[k]$ is given as

$$P_{dBFS} = 10\log_{10}\left(\frac{1}{K}\sum_{k=1}^{K}|y_{rx}[k]|^2\right), \tag{4.9}$$

where K denotes the total number of samples. The difference between the mean values of the measured noise powers occurred as 0.228 dB, which can be neglected. Therefore, the difference in noise powers between Bob and Eve can be ignored when computing the secrecy capacity.

By carrying out a series of measurement experiments, the effect of the RIS on the received signal powers using the algorithm in Figure 4.9 is demonstrated for a location given in Table 4.1, where the RIS is placed at the origin.

Table 4.1. The locations of Alice, Bob, and Eve in meters.

	x	y	z
Alice	0.00	-0.35	0.80
Bob	1.20	-0.35	2.60
Eve	-0.54	-0.35	2.70

A total of 100 measurements are made in an effort to maximize the secrecy capacity, and for each measurement, the order of the elements in the *Steps* is chosen at random. The received signal strengths for Bob and Eve are shown in Figure 4.16 for the location, with dashed lines denoting the average values for each iteration. The boxplots display the first and third quartiles, median, minimum, and maximum of the received signal powers. The results show that, on average, the received power of Bob rises by about 5 dB, while the received power of Eve decreases to the noise floor. The boxplots are used to demonstrate optimizing the RIS with random steps may result in different power levels for Bob and different RIS configurations, however, the overall trend toward increasing Bob's power. The fluctuations that exist in Bob's received power stem from the objective of secrecy capacity in which Eve's power is seen to be more dominant. When Figure 4.17 (a) is analyzed, the objective of increasing the received power of Bob decreases the power fluctuations in power levels. Note that the behaviors of both computer simulation and measurement results in Figures 4.13 and

4.16, respectively, are similar, except Eve's received signal powers saturate at the noise floor in the measurement since the sensitivity of the PLUTO SDR is not sufficient to obtain the signals below 5 dBFS.

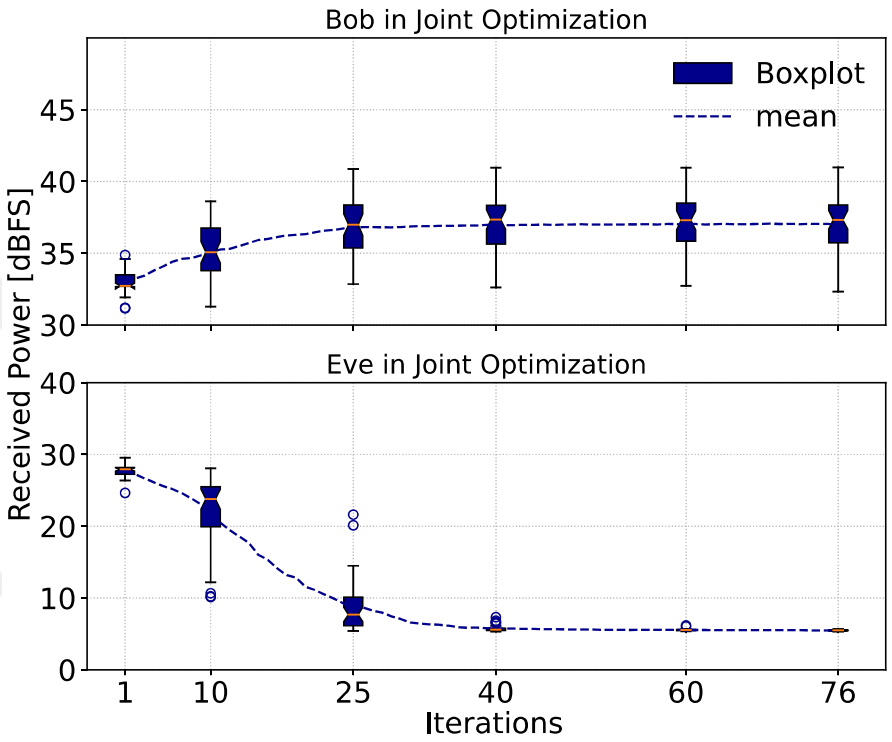

Figure 4.16. Measurement results of the received powers when the objective is to maximize the secrecy capacity.

According to Figure 4.17 (a), when the objective is set to maximize the received power of Bob alone, the received signal power of Bob rises by an average of 14 dB, while when the objective is set to minimize the received power of Eve alone, the received signal power of Eve drops to the noise floor. We observe a similar behavior of the computer simulations such that the received power of Bob fluctuates when the objective is to maximize the secrecy capacity. At the same time, it converges when the aim is to maximize Bob's received power only. As the scattered electric field in Figure 4.11 shows, many regions with low signal powers exist; therefore, the iterative algorithm prioritizes further decreasing Eve's received power to improve the secrecy capacity.

Figure 4.17 (b) shows that the iterative algorithm decreases the Eve's received power significantly and even under the noise floor. Therefore, the power levels do not change with the iterations after some level.

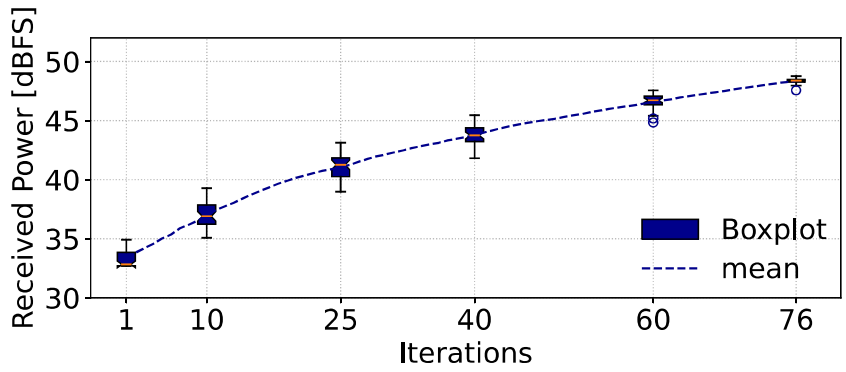

(a)

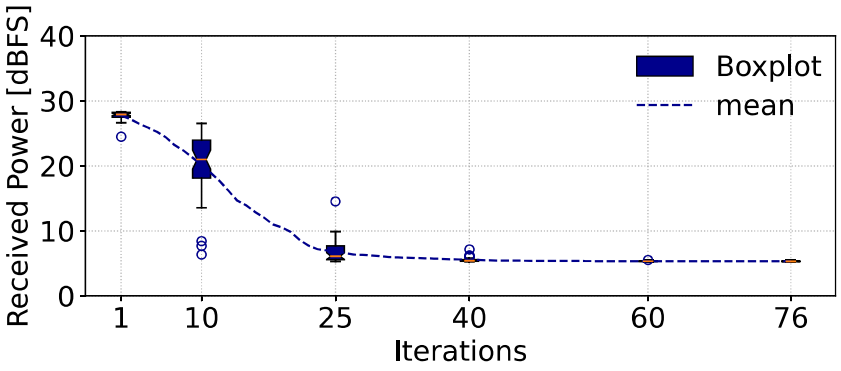

(b)

Figure 4.17. Measurement results of received power of (a) Bob when the objective is to maximize the received power, (b) Eve when the objective is to minimize the received power.

4.2.3.2. Results for Sub-optimal Secrecy Capacity Maximization. The simulation results to demonstrate the impact of the RIS configuration on the received powers of Bob and Eve, where the algorithm given in Figure 4.10 is used for configuring the RIS elements are illustrated in Figure 4.18 and Figure 4.19. Again for the comparison with the before the optimization situation, Figure 4.2 can be used. In Figure 4.18, the scattered radiation pattern of the RIS is illustrated after the optimization according to secrecy capacity with thresholding applied for Eve's received power. When 4.18 (a), is compared with Figure 4.2 (a), it is clearly seen that the RIS gain is directed to Bob, and the gain toward Eve is decreased drastically. However, thresholding for Eve prevents its power from falling much lower than the threshold value. After the optimization, the RIS gain levels for Bob and Eve become 29.7 dB and 17.4 dB, respectively. The RIS gains show us that compromising the RIS gain toward Eve's direction increases the RIS gain toward Bob's direction.

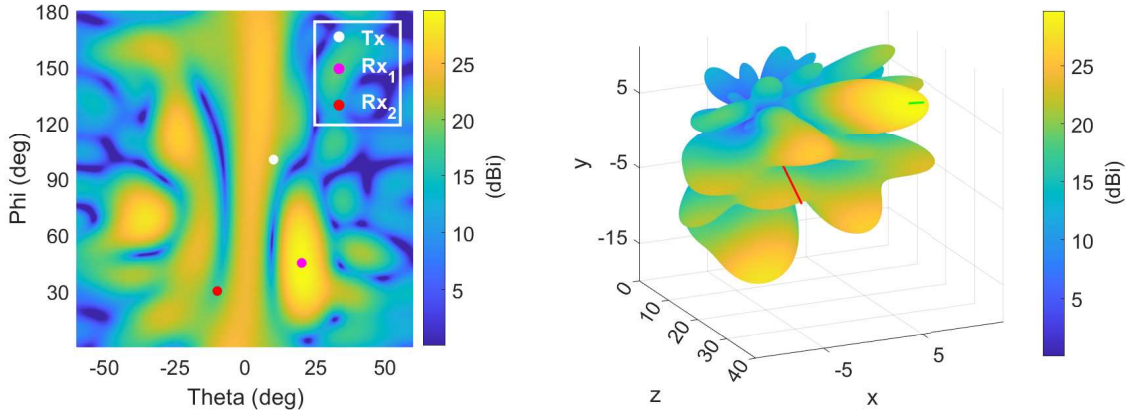

(a) (b)

Figure 4.18. Scattered radiation pattern of the RIS after the coverage optimization with interference minimization under the threshold constraint (a) in terms of azimuth and elevation angles and (b) in terms of cartesian coordinates.

Figure 4.19 illustrates (a) the resulting configuration of the RIS after the optimization and (b) the power changes with respect to iterations. The configuration is somehow similar to the configuration that exists when the RIS is configured according to the secrecy capacity in the previous subsection. The last two rows differentiate with

the configuration that exists in the secrecy capacity maximizing case. Figure 4.19 (b) shows that the iterations corresponding to the last two rows make the received power fluctuate around the threshold level which is defined as 10 dBm. The received powers of Bob and Eve become 26.6 dBm and 11.3 dBm, respectively. As the received power falls down the threshold level, the objective becomes increasing the received power of Bob, and the phases of the RIS defined according to Bob's feedback. However, as soon as Eve's received power rises above the threshold, the objective becomes secrecy capacity again. The behavior can be seen between the iterations 55 and 72. The reason Eve's received power exceeds the threshold level is that defining the phase delay of the RIS element is irrelevant to the new power level Eve can get. Besides, the last steps of the iterations cannot offer a state where the power level of Eve decreases the threshold while maximizing the secrecy capacity.

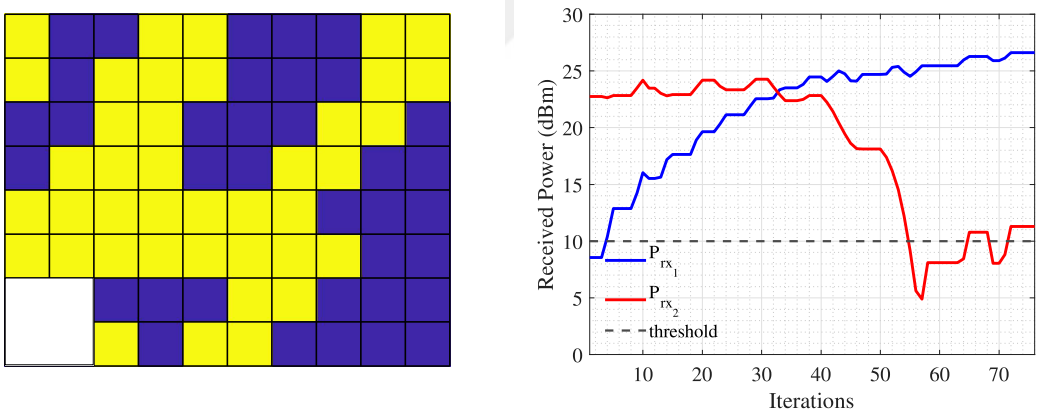

(a) (b)

Figure 4.19. When the coverage optimization is applied by considering maximization of the secrecy capacity with the constraint of a threshold to the unintended receiver, (a) resulting configuration of the RIS (b) the received power levels with respect to iterations.

5. CONCLUSION

In this thesis, first, a detailed literature review of RIS in terms of its fabrication, design improvements, operation modes, use cases, and optimization methods is provided. In the literature review of the optimization methods, it is seen that most of the algorithms utilize channel estimation for the RIS configuration. However, since this thesis focuses on a practical study using a RIS prototype at one stage of the study, one of the most popular methods for configuring the RIS in practical studies, the iterative algorithm, is adopted as a reference algorithm for this thesis. Then, a simulation environment for single-user and multi-user scenarios is built in MATLAB environment for coverage enhancement in NLOS conditions.

The thesis can be investigated in two main parts. In the first part, a RIS optimization method that combines the iterative method with CNN for a single-user scenario is proposed. The proposed method is evaluated numerically, and comparisons with the iterative algorithm are provided. Also, to demonstrate the performance of the CNN model, the result corresponding to the comparison of consecutive horizontal and vertical grouping and the iterative algorithm is also provided. The results show that the proposed method achieves a very high performance (close to that of the iterative algorithm) while reducing the number of iterations from $N \times M$ to $N + M$.

In the second part, coverage enhancement in two-user scenarios is investigated under two main headings. First, the aim is to enhance the coverage for two users simultaneously, where the objective of the algorithm is chosen according to the RIS gain distribution corresponding to the users. Fair and prioritized gain distributions are investigated in this context. The corresponding radiation pattern of the RIS with 2D and 3D forms is provided. Also, the resulting configuration of the RIS and the received power changes with respect to iterations are also provided. Secondly, the goal of the RIS-assisted communication system becomes coverage enhancement for one user while interference mitigation for the other user. The RIS can be utilized in this context for

maximizing the secrecy capacity or decreasing Eve's received power under a threshold level while maximizing the secrecy capacity. For the former objective, the results show that Eve's received power becomes dominant and the RIS is configured according to Eve generally. In the latter one, the thresholding weakens the dominance of Eve which enables Bob's received power to increase in return for sacrificing the secrecy capacity. Finally, a RIS prototype has been utilized in a wireless communication system in order to increase the secrecy capacity between Bob and Eve. Both measurement and computer simulation results show that the secrecy capacity can be significantly improved by employing the RIS in an indoor environment. This improvement is obtained by assuming that the received power of Eve is available, which may not be true for practical scenarios.

To sum up, we have proposed a RIS optimization method for a single-user communication system. The analysis demonstrates that RIS configuring with a deep-learning model can quicken the optimization process with minor performance losses. Additionally, we have demonstrated RIS utilization in a two-user communication system, where the RIS can serve for both joint coverage enhancement or coverage enhancement with interference mitigation. Finally, we have provided practical measurements for secrecy capacity maximization and showed the simulation and measurement results are consistent.

5.1. Future Work

For the first part of this thesis, to further improve the performance, especially in the higher elevation regions, different learning models can be developed and evaluated. Besides, multi-user cases are significant scenarios that require to be investigated, as well as some sensing applications like the angle of arrival estimation. Additionally, experimental studies can also be conducted for more realistic results and practical issues.

For the second part, link management for multi-user (more than two) is an important problem and needed to be examined in detail. Moreover, although the initial results for providing PLS with RIS are promising, future work will investigate how these results can be achieved for real-life deployments.

REFERENCES

1. Goldsmith, A., *Wireless Communications*, Cambridge University Press, Cambridge, 2005.

2. Di Renzo, M., A. Zappone, M. Debbah, M.-S. Alouini, C. Yuen, J. de Rosny and S. Tretyakov, "Smart Radio Environments Empowered by Reconfigurable Intelligent Surfaces: How It Works, State of Research, and The Road Ahead", *IEEE Journal on Selected Areas in Communications*, Vol. 38, No. 11, pp. 2450–2525, 2020.

3. Cai, C., X. Yuan, W. Yan, Z. Huang, Y.-C. Liang and W. Zhang, "Hierarchical Passive Beamforming for Reconfigurable Intelligent Surface Aided Communications", *IEEE Wireless Communications Letters*, Vol. 10, No. 9, pp. 1909–1913, 2021.

4. Zhang, Z., L. Dai, X. Chen, C. Liu, F. Yang, R. Schober and H. V. Poor, "Active RIS vs. Passive RIS: Which Will Prevail in 6G?", *IEEE Transactions on Communications*, 2022.

5. Zhi, K., C. Pan, H. Ren, K. K. Chai and M. Elkashlan, "Active RIS Versus Passive RIS: Which Is Superior with the Same Power Budget?", *IEEE Communications Letters*, Vol. 26, No. 5, pp. 1150–1154, 2022.

6. Yildirim, I., F. Kilinc, E. Basar and G. C. Alexandropoulos, "Hybrid RIS-Empowered Reflection and Decode-and-Forward Relaying for Coverage Extension", *IEEE Communications Letters*, Vol. 25, No. 5, pp. 1692–1696, 2021.

7. Team, E. C., "ETSI Releases First Use Cases for Reconfigurable Intelligent Surface", 2023, `https://www.etsi.org/newsroom/press-releases`, accessed on June 1, 2023.

8. Nemati, M., J. Park and J. Choi, "RIS-Assisted Coverage Enhancement in

Millimeter-Wave Cellular Networks", *IEEE Access*, Vol. 8, pp. 188171–188185, 2020.

9. Arun, V. and H. Balakrishnan, "RFocus: Practical Beamforming for Small Devices", *arXiv preprint arXiv:1905.05130*, 2019.

10. Trichopoulos, G. C., P. Theofanopoulos, B. Kashyap, A. Shekhawat, A. Modi, T. Osman, S. Kumar, A. Sengar, A. Chang and A. Alkhateeb, "Design and Evaluation of Reconfigurable Intelligent Surfaces in Real-World Environment", *IEEE Open Journal of the Communications Society*, Vol. 3, pp. 462–474, 2022.

11. Dai, L., B. Wang, M. Wang, X. Yang, J. Tan, S. Bi, S. Xu, F. Yang, Z. Chen, M. D. Renzo, C.-B. Chae and L. Hanzo, "Reconfigurable Intelligent Surface-Based Wireless Communications: Antenna Design, Prototyping, and Experimental Results", *IEEE Access*, Vol. 8, pp. 45913–45923, 2020.

12. Liang, J. C., Q. Cheng, Y. Gao, C. Xiao, S. Gao, L. Zhang, S. Jin and T. J. Cui, "An Angle-Insensitive 3-Bit Reconfigurable Intelligent Surface", *IEEE Transactions on Antennas and Propagation*, Vol. 70, No. 10, pp. 8798–8808, 2022.

13. You, L., J. Xiong, D. W. K. Ng, C. Yuen, W. Wang and X. Gao, "Energy Efficiency and Spectral Efficiency Tradeoff in RIS-Aided Multiuser MIMO Uplink Transmission", *IEEE Transactions on Signal Processing*, Vol. 69, pp. 1407–1421, 2020.

14. Basar, E., M. Di Renzo, J. De Rosny, M. Debbah, M.-S. Alouini and R. Zhang, "Wireless Communications Through Reconfigurable Intelligent Surfaces", *IEEE Access*, Vol. 7, pp. 116753–116773, 2019.

15. Wu, Q. and R. Zhang, "Towards Smart and Reconfigurable Environment: Intelligent Reflecting Surface Aided Wireless Network", *IEEE Communications Magazine*, Vol. 58, No. 1, pp. 106–112, 2020.

16. Rajatheva, N., I. Atzeni, E. Bjornson, A. Bourdoux, S. Buzzi, J.-B. Dore, S. Erkucuk, M. Fuentes, K. Guan, Y. Hu, X. Huang, J. Hulkkonen, J. M. Jornet, M. Katz, R. Nilsson, E. Panayirci, K. Rabie, N. Rajapaksha, M. Salehi, H. Sarieddeen, T. Svensson, O. Tervo, A. Tolli, Q. Wu and W. Xu, "White paper on broadband connectivity in 6G", *arXiv preprint arXiv:2004.14247*, 2020.

17. Zhang, S. and R. Zhang, "Capacity Characterization for Intelligent Reflecting Surface Aided MIMO Communication", *IEEE Journal on Selected Areas in Communications*, Vol. 38, No. 8, pp. 1823–1838, 2020.

18. Mu, X., Y. Liu, L. Guo, J. Lin and N. Al-Dhahir, "Capacity and Optimal Resource Allocation for IRS-Assisted Multi-User Communication Systems", *IEEE Transactions on Communications*, Vol. 69, No. 6, pp. 3771–3786, 2021.

19. Wu, Q. and R. Zhang, "Intelligent Reflecting Surface Enhanced Wireless Network via Joint Active and Passive Beamforming", *IEEE Transactions on Wireless Communications*, Vol. 18, No. 11, pp. 5394–5409, 2019.

20. Huang, C., A. Zappone, G. C. Alexandropoulos, M. Debbah and C. Yuen, "Reconfigurable Intelligent Surfaces for Energy Efficiency in Wireless Communication", *IEEE Transactions on Wireless Communications*, Vol. 18, No. 8, pp. 4157–4170, 2019.

21. Wu, Q. and R. Zhang, "Intelligent Reflecting Surface Enhanced Wireless Network: Joint Active and Passive Beamforming Design", *2018 IEEE Global Communications Conference (GLOBECOM)*, Abu Dhabi, United Arab Emirates, 2018.

22. Faisal, A., I. Al-Nahhal, O. A. Dobre and T. M. N. Ngatched, "Deep Reinforcement Learning for Optimizing RIS-Assisted HD-FD Wireless Systems", *IEEE Communications Letters*, Vol. 25, No. 12, pp. 3893–3897, 2021.

23. Abdallah, A., A. Celik, M. M. Mansour and A. M. Eltawil, "Deep Reinforcement

Learning Based Beamforming Codebook Design for RIS-aided mmWave Systems", *2023 IEEE 20th Consumer Communications and Networking Conference (CCNC)*, pp. 1020–1026, 2023.

24. Li, L., D. Ma, H. Ren, D. Wang, X. Tang, W. Liang and T. Bai, "Enhanced Reconfigurable Intelligent Surface Assisted mmWave Communication: A Federated Learning Approach", *China Communications*, Vol. 17, No. 10, pp. 115–128, 2020.

25. Peng, Z., T. Li, C. Pan, H. Ren, W. Xu and M. D. Renzo, "Analysis and Optimization for RIS-Aided Multi-Pair Communications Relying on Statistical CSI", *IEEE Transactions on Vehicular Technology*, Vol. 70, No. 4, pp. 3897–3901, 2021.

26. Gros, J.-B., V. Popov, M. A. Odit, V. Lenets and G. Lerosey, "A Reconfigurable Intelligent Surface at mmWave Based on a Binary Phase Tunable Metasurface", *IEEE Open Journal of the Communications Society*, Vol. 2, pp. 1055–1064, 2021.

27. Kayraklık, S., I. Yildirim, Y. Gevez, E. Basar and A. Görçin, "Indoor Coverage Enhancement for RIS-Assisted Communication Systems: Practical Measurements and Efficient Grouping", *arXiv preprint arXiv:2211.07188*, 2022.

28. Keşir, S., S. Kayraklık, İ. Hökelek, A. E. Pusane, E. Basar and A. Görçin, "Measurement-Based Characterization of Physical Layer Security for RIS-assisted Wireless Systems", *arXiv preprint arXiv:2212.07254*, 2022.

29. Pei, X., H. Yin, L. Tan, L. Cao, Z. Li, K. Wang, K. Zhang and E. Björnson, "RIS-Aided Wireless Communications: Prototyping, Adaptive Beamforming, and Indoor/Outdoor Field Trials", *IEEE Transactions on Communications*, Vol. 69, No. 12, pp. 8627–8640, 2021.

30. Yang, Y., S. Zhang and R. Zhang, "IRS-Enhanced OFDMA: Joint Resource Allocation and Passive Beamforming Optimization", *IEEE Wireless Communications Letters*, Vol. 9, No. 6, pp. 760–764, 2020.

31. Yan, W., X. Yuan and X. Kuai, "Passive Beamforming and Information Transfer via Large Intelligent Surface", *IEEE Wireless Communications Letters*, Vol. 9, No. 4, pp. 533–537, 2020.

32. Tan, X., Z. Sun, J. M. Jornet and D. Pados, "Increasing Indoor Spectrum Sharing Capacity Using Smart Reflect-Array", *2016 IEEE International Conference on Communications (ICC)*, pp. 1–6, Kuala Lumpur, Malaysia, 2016.

33. Arun, V. and H. Balakrishnan, "RFocus: Beamforming Using Thousands of Passive Antennas", *17th USENIX Symposium on Networked Systems Design and Implementation (NSDI 20)*, pp. 1047–1061, Santa Clara, CA, 2020.

34. Wang, Z., L. Tan, H. Yin, K. Wang, X. Pei and D. Gesbert, "A Received Power Model for Reconfigurable Intelligent Surface and Measurement-Based Validations", *IEEE 22nd International Workshop on Signal Processing Advances in Wireless Communications (SPAWC)*, pp. 561–565, Lucca, Italy, 2021.

35. Gao, B., J. Li, Z. Yu, J. Sang, M. Zhou, J. Lan, W. Tang, X. Li and S. Jin, "Propagation Characteristics of RIS-assisted Wireless Channels in Corridors: Measurements and Analysis", *IEEE/CIC International Conference on Communications in China (ICCC)*, pp. 550–554, Sanshui, Foshan, China, 2022.

36. Xu, W., J. Zhang, S. Cai, J. Wang and Y. Wu, "RIS-assisted MIMO Secure Communications with Bob's Statistical CSI and without Eve's CSI", *Digital Communications and Networks*, Vol. 9, No. 3, pp. 638–644, 2022.

37. Zhang, J., H. Du, Q. Sun, B. Ai and D. W. K. Ng, "Physical Layer Security Enhancement with Reconfigurable Intelligent Surface-Aided Networks", *IEEE Transactions on Information Forensics and Security*, Vol. 16, pp. 3480–3495, 2021.

38. Yang, L., J. Yang, W. Xie, M. O. Hasna, T. Tsiftsis and M. D. Renzo, "Secrecy Performance Analysis of RIS-Aided Wireless Communication Systems", *IEEE Trans-*

actions on Vehicular Technology, Vol. 69, No. 10, pp. 12296–12300, 2020.

39. Zhou, G., C. Pan, H. Ren, K. Wang and Z. Peng, "Secure Wireless Communication in RIS-Aided MISO System With Hardware Impairments", *IEEE Wireless Communications Letters*, Vol. 10, No. 6, pp. 1309–1313, 2021.

40. Yang, H., X. Cao, F. Yang, J. Gao, S. Xu, M. Li, X. Chen, Y. Zhao, Y. Zheng and S. Li, "A Programmable Metasurface with Dynamic Polarization, Scattering and Focusing Control", *Scientific Reports*, Vol. 6, No. 1, pp. 1–11, 2016.

41. Chollet, F., "Keras", `https://github.com/fchollet/keras`, 2015, accessed on May 20, 2023.

42. "Greenerwave 2022, 35 rue du Sentier, 75002 Paris, France", `https://greenerwave.com/`, 2022, accessed on May 15, 2023.

43. Ayhan, M., Y. Zhao and H.-A. Choi, "Utilizing Geometric Mean in Proportional Fair Scheduling: Enhanced Throughput and Fairness in LTE DL", *2016 IEEE Global Communications Conference (GLOBECOM)*, Washington, DC, USA, 2016.

44. Wang, T. and L. Vandendorpe, "Iterative Resource Allocation for Maximizing Weighted Sum Min-Rate in Downlink Cellular OFDMA Systems", *IEEE Transactions on Signal Processing*, Vol. 59, No. 1, pp. 223–234, 2011.

45. Cui, M., Z. Wu, Y. Lu, X. Wei and L. Dai, "Near-Field MIMO Communications for 6G: Fundamentals, Challenges, Potentials, and Future Directions", *IEEE Communications Magazine*, Vol. 61, No. 1, pp. 40–46, 2023.